

HIGH RESOLUTION MEASUREMENTS OF SHELL-SIDE VELOCITY FIELDS IN
HELICAL COIL STEAM GENERATORS USING PARTICLE IMAGE VELOCIMETRY

A Thesis

by

MARILYN IRENE DELGADO

Submitted to the Office of Graduate and Professional Studies of
Texas A&M University
in partial fulfillment of the requirements for the degree of

MASTER OF SCIENCE

Chair of Committee,	Yassin A. Hassan
Committee Members,	Rodolfo Vaghetto
	Maria King

Head of Department,	Yassin A. Hassan
---------------------	------------------

May 2018

Major Subject: Nuclear Engineering

Copyright 2018 Marilyn Irene Delgado

ABSTRACT

The helical coil steam generator is a type of tube and shell heat exchanger that is proposed for many small modular and Gen IV reactor designs. It is favored due to the higher heat transfer it provides compared to traditional U-tube steam generators, compact design and thermal stress flexibility. The arrangement of tubes, where the secondary two-phase fluid flows, determines the shell side, pressurized single phase flow. This study focuses on the fluid structures that form in the shell side flow when adjacent helical tube bundles coil in opposite directions. Two helical coil steam generator designs were created and studied using a high-resolution flow visualization technique, refractive index matching particle image velocimetry (PIV). Experiments focused on multiple planes across each test section for different lateral pitch tube arrangements at $Re \sim 8,500$. Two-dimensional image sequences captured with a high speed camera were processed to determine average velocity flow fields for x- and y-direction velocity components. Two main regions of flow develop between tube bundle arrangements, center streamline flow and recirculation regions below the tubes. Previous studies have shown these recirculation regions are responsible for the increase in heat transfer this geometry offers. Nevertheless, vortices that form in these regions have the potential to grow and enter the streamline, a phenomenon called vortex shedding. The frequency of this shedding behavior is currently correlated to lateral and transverse pitches between bundles. A comparative study showed that while the center streamline development remained consistent between helical coil steam generator models, the recirculation regions varied in strength and relative size. Areas with a larger lateral pitch, expected to have large recirculation development between the rods, did not have the highest velocity magnitude. These average velocity fields suggest that relative location

along the coiling bundle also contributes to the vortex shedding behavior of the recirculation regions below the tubes. Future work aims to study the transient behavior of the flow to have an in-depth analysis of the relationship between lateral pitch, transverse pitch, radial location around the helical coil tube bundle and recirculation region development.

DEDICATION

This work is dedicated to my mother, Ines Eulalia Abarca Alvarez. From a young age you always prioritized education, whether it was bringing me to the library after-school or going back to school yourself to become a medical assistant. Your hard work, kindness and appreciation of education did not go un-noticed. Thank you for being an excellent role model and for all your support throughout my life.

ACKNOWLEDGEMENTS

I would like to thank my committee chair, Dr. Yassin A. Hassan for his patience, guidance and constant support throughout my research endeavors. I would like to thank my committee member Dr. Rodolfo Vaghetto for his invaluable every day support and understanding to my endless questions. I would also like to thank Dr. Maria King for being an exemplary role model and for her support of my research. Outside of my committee, I would like to express my gratitude for Dr. Saya Lee who dedicated the time and effort to teach me how to be a diligent researcher. Also, Dr. NK Anand for his support and knowledge during the countless revisions of my published work and Dr. Thien Nguyen for his support and advice along my research.

This research would not be possible if it not were for a team of individuals that helped in the construction, collection and processing of data for both facilities. My greatest appreciation is to Garland A. Porter and Michael S. Gorman both whom started this project with me. To the following undergraduate students, I thank you for your help, Robert M. Heath, Rami Mooti, Elliott Gorman, Joshua McGuire, Arturo Cabral, Colin Guilbault, Ross Winningham, and Stephen King. Thank you to my colleagues at the Nuclear Engineering Thermal-Hydraulics research laboratory and the department faculty and staff for making my time at Texas A&M University a great experience.

Finally, I would like to thank Emina Djukanovic, Brian R. Mosquera, Joshua S. Milian and Julio Trujillo who have been by my side for many years and remain my closest friends through this journey of life.

CONTRIBUTORS AND FUNDING SOURCES

This work was supported by a dissertation committee consisting of Professor Yassin A. Hassan, as an advisor, and Dr. Rodolfo Vaghetto of the Department of Nuclear Engineering and Dr. Maria King of the Department of Biological and Agricultural Engineering. This work was financially supported from Argonne National Laboratory through the Nuclear Energy Advanced Modeling and Simulation (NEAMS) program of the Department of Energy (DOE). All work for the thesis was completed independently by the student.

NOMENCLATURE

a	Transverse Pitch Ratio
b	Lateral Pitch Ratio
d	Diameter
HCSG	Helical Coil Steam Generator
N	number of PIV frames
PIV	Particle Image Velocimetry
R	residual
Re	Reynolds Number
S	Pitch
St	Stokes Number
Δt	PIV image time interval
U	Velocity in the x-direction, transverse velocity
V	Velocity in the y-direction, vertical velocity
ΔX	PIV image displacement
α	magnification factor
δu	PIV image difference factor
ρ	density
μ	p-cymene viscosity at working temperature
σ	uncertainty/ standard deviation

Subscripts

b	lateral pitch ratio
C	combined
H	helical coil bundle
i	location along x-axis
j	location along y-axis
L	lateral
MAX	maximum
MIN	minimum
N	normalized to inlet velocity
P	seeding particle
PIV	particle image velocimetry
R	rod/tube
ST	streamwise region
T	transverse
W	wake region
1	relating to Test Section I
2	relating to Test Section II
∞	inlet/ free stream

TABLE OF CONTENTS

	Page
ABSTRACT.....	ii
DEDICATION.....	iv
ACKNOWLEDGEMENTS.....	v
CONTRIBUTORS AND FUNDING SOURCES.....	vi
NOMENCLATURE.....	vii
TABLE OF CONTENTS.....	ix
LIST OF FIGURES.....	xi
LIST OF TABLES.....	xiv
CHAPTER I INTRODUCTION.....	1
CHAPTER II DESIGN AND CONSTRUCTION OF EXPERIMENTAL TEST FACILITIES.....	7
CHAPTER III EXPERIMENTAL METHOD.....	15
Regions of Interest.....	15
Particle Image Velocimetry (PIV) Set-Up and Method.....	17
Test Section I PIV Frames.....	19
Test Section I PIV Frame Analysis.....	20
Test Section II PIV Frames.....	21
Test Section II PIV Frame Analysis.....	23
PIV Averaging and Uncertainty.....	25
CHAPTER IV TEST SECTION I RESULTS.....	28
CHAPTER V TEST SECTION II RESULTS.....	34
CHAPTER VI DISCUSSION AND CONCLUSIONS.....	40
Comparison and Discussion.....	40

Conclusions.....	45
REFERENCES.....	47

LIST OF FIGURES

		Page
Figure 1	Typical U-Tube cross-flow tube and shell heat exchanger used in Nuclear Power Plants.....	2
Figure 2	In-line and Staggered Tube Geometries.....	4
Figure 3	An inline and staggered tube arrangement with characteristic properties.....	8
Figure 4	Design of a helical coil steam generator starting from a) a single helical tube bundle, b) two counter-coiling tube bundles and c) a series of concentric helically coiling tube bundles.....	9
Figure 5	Design of two inter-coiling tube bundles and region of interest for Test Section I.....	9
Figure 6	Design of five inter-coiling tube bundles and region of interest for Test Section II.....	10
Figure 7	CAD models of Test Section I and II.....	12
Figure 8	Honeycomb and screen assembly using silicone adhesive of Test Facility I.....	13
Figure 9	a) Test Section I and b) Test Section II experimental facilities.....	14
Figure 10	Test Section I and II with cross-sectional planes of interest.....	15
Figure 11	An example of an image captured in Test Section II with a perpendicular camera and laser set-up.....	16
Figure 12	Test Section II new planes defined for PIV image capture.....	17
Figure 13	Test Section II filled with p-cymene and air to demonstrate refractive index matching.....	17
Figure 14	Test Section I plane 1A and a sample frame.....	20
Figure 15	Scheimpflug Lens Camera and Laser PIV Set-up on Test Section II.....	21

Figure 16	Test Section II example PIV frame captured using Scheimpflug Lens.....	22
Figure 17	An original image taken with the Scheimpflug lens and its corrected form.....	23
Figure 18	Test Section I plane and the 4 frame areas. Across each of the three planes, four frame heights were taken for a total of 12 frames in Test Section I for average velocity fields.....	28
Figure 19	Crossflow fluid structures within Test Section I.....	29
Figure 20	Velocity in the x-direction, U (mm/s), for Test Section I planes.....	30
Figure 21	Velocity in the y-direction, V (mm/s), for Test Section I planes.....	32
Figure 22	Test Section II planes and the 2 frame areas. Across each of the three planes, two frame heights were taken for a total of 6 frames in Test Section II.....	34
Figure 23	Cross-flow fluid structures within Test Section II.....	35
Figure 24	Velocity in the x-direction, U (mm/s), for Test Section II planes...	37
Figure 25	Velocity in the y-direction, V (mm/s), for Test Section II planes...	39
Figure 26	Extrema as a function of Lateral Pitch Ratio for (a) transverse and (b) vertical velocity components.....	41
Figure 27	Normalized maximum and minimum transverse velocity as a function of Lateral Pitch Ratio for (a) Test Section I and (b) Test Section II.....	42
Figure 28	An example of the wake and streamline regions within the planes of interest in Test Section I and II.....	43

LIST OF TABLES

		Page
Table I	Test Section I and II Design Characteristics.....	14
Table II	Test Section II Corrected Image Properties.....	24
Table III	Uncertainty Properties for Test Section I and II.....	27
Table IV	Characteristic x-direction velocity, U (mm/s), for Test Section I.....	31
Table V	Characteristic y-direction velocity, V (mm/s), for Test Section I.....	33
Table VI	Test Section II average lateral pitch ratio and standard deviations per plane.....	35
Table VII	Characteristic x-direction velocity, U (mm/s), for Test Section II....	37
Table VIII	Characteristic y-direction velocity, V (mm/s), for Test Section II....	39
Table IX	Lateral Pitch Ratio, b, for each plane across Test Section I and II....	40
Table X	Average Streamline and Wake velocity intensity for the fifth rod row in TS I and II.....	43

CHAPTER I

INTRODUCTION*

The helical coil steam generator (HCSG) is a type of heat exchanger that since the 1940's has been investigated to provide higher heat transfer between its primary and secondary flow than heat exchangers of similar geometry [1]. In any field where the exchange of heat is beneficial, for example, chemical, industrial, and petroleum fields, the helical coil steam generator has been developed and used. In the field of nuclear engineering, the helical coil steam generator has seen an increase in attention as the next generation of nuclear reactors, sodium-cooled fast reactors, high temperature reactors, and small modular reactors (SMR) propose to use this design [2, 3, 4, 5]. Many of these new designs incorporate a type of helical coil steam generator for its increased heat transfer, compact design and thermal stress flexibility.

Different types of heat exchangers serve different purposes based on the type of fluids and heat transfer specifications. Heat exchangers can be categorized by their flow arrangement and their geometry. Flow between two fluids is characterized by their orientation to one another, namely parallel-flow, counter-flow and crossflow. Heat exchangers are designed to optimize the amount of surface area between the two fluids. Geometries of heat exchangers depend on material, space and cost [6]. Different geometries include tube and shell, plate, microchannel, direct contact and spiral heat exchangers where the addition of fins and corrugations help to increase the surface area between the two fluids. One of the most common types and engineered designs of heat

* Reprinted with permission from “Flow visualization study at the interface of alternating pitch tube bundles in a model helical coil steam generator using particle image velocimetry” by Marilyn Delgado, Saya Lee, Yassin Hassan, and N.K Anand, 2018. *International Journal of Heat and Mass Transfer*, 122, 614 – 628, Copyright 2018 by Elsevier.

exchangers for high pressure applications is the tube and shell heat exchanger design. Figure 1 shows the most common type of cross-flow tube and shell heat exchanger used in current nuclear power plants, the U-tube heat exchanger. It uses the water coming from the core, or primary fluid side, to transfer heat to a secondary side, or feedwater flow. The primary side is divided into a bundle of hollow tubes and gives off heat to the feedwater flow side within the shell, forming a U-shape. The feedwater, or secondary side flow is heated until saturation and becomes steam.

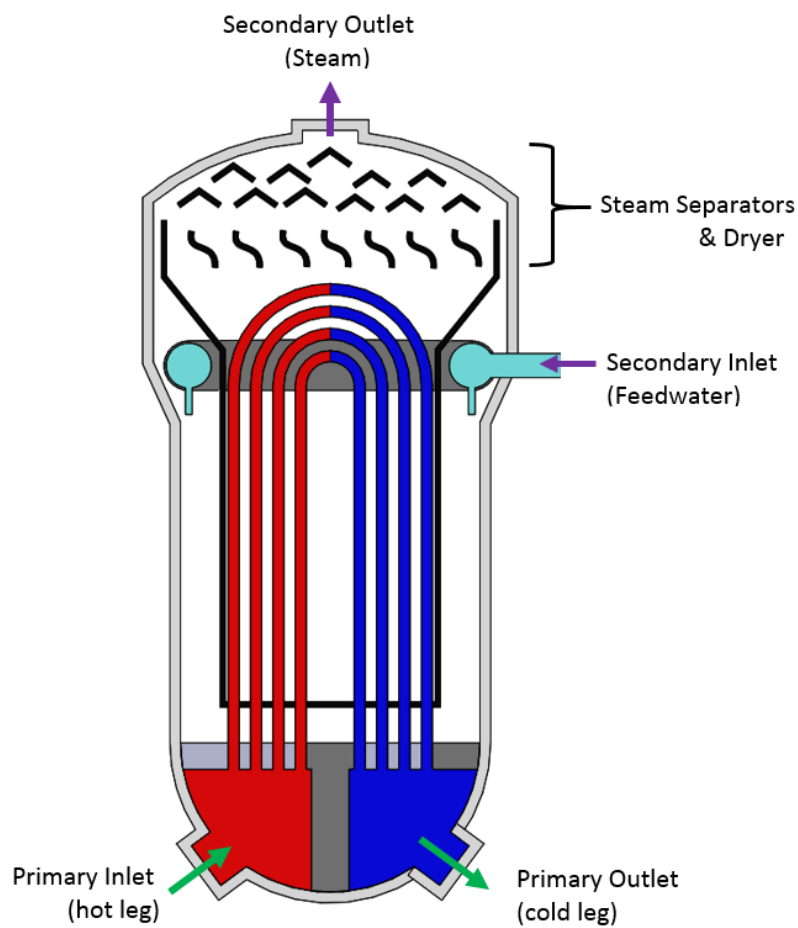


Figure 1 - Typical U-Tube cross-flow tube and shell heat exchanger used in Nuclear Power Plants

A helical coil heat exchanger was first used in the nuclear industry in the 1970's for transferring heat in a liquid metal fast breeder reactor. Since this time, the helical coil heat

exchanger has been studied and proposed with using water as the primary and secondary fluid. An advantage to using water as the secondary fluid is that it can be converted to superheated steam while passing through the heat exchanger and fed directly into the steam separator, as the U-tube heat exchanger discussed earlier. Therefore, the helical coil heat exchanger is then more commonly referred to as a helical coil steam generator (HCSG). Unlike in the U-tube heat exchanger, future nuclear power plants look at a HCSG design where the shell side flow is the primary, single-phase fluid, and within the tubes is the secondary side, where water will turn into superheated steam [2, 3, 4, 5].

Tube and shell heat exchangers depend on the geometry of the design to optimize heat transfer. The number of tubes influences the amount of surface area that a fluid is able to interact with the other. As seen in the U-tube heat exchanger, the shell side fluid flows along-side the tubes for parallel flow. A way to further increase heat transfer from the shell side is to increase the turbulence or increase the mixing of the fluid. The shell side fluid in a HCSG is characterized by the cross-flow fluid patterns allowed by the arrangement of the tubes. These tube configurations are defined based on the center-to-center distances across tubes in a bundle and tube bundle geometry. The two most common configurations are in-line and staggered tubes in straight bundles. Figure 2 presents the in-line and staggered tube bundle geometry. The HCSG provides many advantages over straight tube and shell models. Primarily, it provides a higher heat transfer area per unit volume. The helix design has demonstrated an increase of 16 to 43% higher heat transfer than a straight tube bundle [1]. Due to its design, it is also able to better withstand thermal expansion during transient behavior, the limitations of which are now a topic for research based on different accident scenarios [7]. The interest in the helical coil steam generator has lead a multitude of

researchers to study the helical coil steam generator although the majority of these studies focus on the simple geometries of the heat exchanger, in-line and staggered.

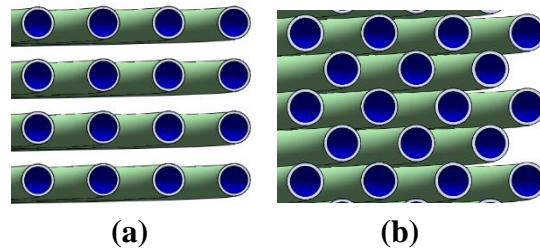


Figure 2 – (a) In-line and (b) Staggered Tube Geometry

One of the earliest studies of flow visualization within in-line and staggered tube bundles demonstrated alternate shedding eddies [8] that lead to an increase of interest in the effects of cross-flow structures over tube bundles. Bradshaw [9] performed smoke visualization within a single row of tubes and noted that the flow behind tubes of a single row were non-uniform although they had constant pitch. Zdravkovich [10] observed flow patterns and pressure distribution across tube arrays and suggested that flow induced vibration was responsible for the variation. Studies such as by Weaver and Avd-Rabbo [11] observed symmetric vortex shedding that was related to the tube vibration but lacked quantitative evaluation. Experimental velocity data from the interstitial flow became a necessary component for the design of heat exchangers. Aiba et al. [12] made velocity measurements using hot-wire anemometry and found that heat transfer coefficients were dependent on tube configuration, determining the changes were a result of velocity and turbulence characteristics. Velocity measurements done with Laser Doppler Anemometry (LDA) by Simonin and Barcouda [13] then compared the results to $k-\epsilon$ model simulations. Balabani and

Yianneskis [14] also made LDA measurements to compare in-line and staggered tube bundles but the measurement points were limited. With increased computing capabilities, large eddy simulations and numerical simulations across tube bundles have become accessible which delineate the flow-induced vibration phenomena. A more comprehensive overview of simulation progress in fluid flow analysis is covered by Hoffer [3], Hassan [15], and Sweeny [16]. Nevertheless, they are limited by either the simplifications needed in order to make the computation resolution reasonable or lack detailed experimental data to compare. Attempts to resolve experimental data and two-phase pressure drop correlations have also demonstrated the need for a more comprehensive analysis of the flow field behavior contributing to heat transfer between shell and tube side flows [17]. Effective predictions of flow across tube bundles are important to their design, but with the variety of designs currently in practice, it has been difficult to analyze flow patterns based on individual geometric parameters. A comprehensive historical summary and discussion on the characteristics of flow and heat transfer for tube bundles can be found by authors Zukauskas and Ulinskas [18].

Flow visualization techniques have advanced. One technique which provides full field measurements of the velocity components with emphasis on particle tracking is known as Particle Image Velocimetry (PIV). This technique offers an advantage by looking at an area rather than a single point measurement, such as those done with LDA and hot-wire anemometry. In recent years, researchers such as Paul [19], Iwaki [20], and Konstantinidis [21] among others have used PIV to study in-line and staggered tube bundles. Literature review of multiple proposed helical coil steam generator designs lead the authors to a HCSG design with multiple concentric helix bundles of alternating helical pitches [3, 4, 22, 23]. Unlike the in-line and staggered tube bundles, a design with alternating helical pitches will have areas repeating radially where the tubes are neither inline

or staggered but changing periodically. This unique coiling behavior has been investigated to induce higher turbulence in the shell side flow but can also create large fluid structures that within the shell could lead to fluid induced vibrations. There are several studies that utilize computational methods to predict these types of complex flow fields of alternating helical pitches [24 and 25]. Nevertheless, without experimental data, it is difficult to validate the results these studies provide.

This study examines the unique coiling behavior of a helical coil steam generator design and uses particle image velocimetry to visualize the flow structures within them. Two test sections were constructed to study the shell side flow and flow fields were captured at different planes along their coiling bundles. The fluid structures and average velocity intensities of each are analyzed and compared to give insight into the influence the geometry has on the shell side fluid in the steam generator design.

CHAPTER II

DESIGN AND CONSTRUCTION OF EXPERIMENTAL TEST FACILITIES*

Cross-flow behavior within the shell side of a HCSG is highly dependent on the geometry of the tubes. As discussed previously, the shell side flow within the HCSG design presented in this study is the pressurized single phase flow. This flow will develop around the tube bundles, making their geometry important to the design of the heat exchanger. For the majority of heat exchangers that are designed with helical coil tube bundles, the bundle divides the fluid evenly into its tubes and coils together all concentric bundles in a particular direction for the length of the heat exchanger. The geometry between the tubes is either considered in-line or staggered based on center-to-center distances between adjacent tubes. Figure 3 demonstrates the characteristic tube geometry and its properties for both patterns. An in-line geometry is one where adjacent tubes align with one another and form a quadrilateral while staggered tubes form a triangle between adjacent rows. The transverse, a , and stream-wise or lateral, b , tube pitch-to-diameter ratios are defined as

$$a = \frac{S_T}{d_R} \quad \text{Eq 1.}$$

$$b = \frac{S_L}{d_R} \quad \text{Eq 2.}$$

* Reprinted with permission from “Flow visualization study at the interface of alternating pitch tube bundles in a model helical coil steam generator using particle image velocimetry” by Marilyn Delgado, Saya Lee, Yassin Hassan, and N.K Anand, 2018. *International Journal of Heat and Mass Transfer*, 122, 614 – 628, Copyright 2018 by Elsevier.

where d_R is the rod/tube diameter, S_T is the transverse pitch, and S_L is the lateral pitch. Tube bundles are most commonly in-line square with $a=b$, or staggered with an equilateral triangle arrangement where $a=2b/\sqrt{3}$ [26].

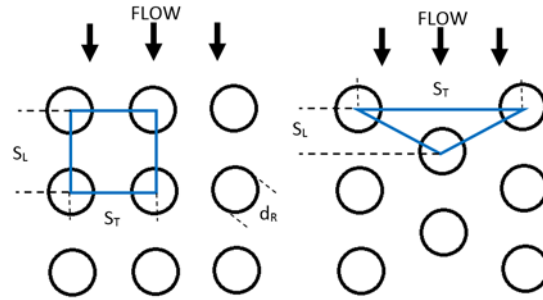


Figure 3 – An inline and staggered tube arrangement with characteristic properties

The discussed designs for nuclear applications have inter-coiling bundles, meaning they are neither in-line or staggered. A tube bundle described in Figure 4a, coils in a clockwise direction with a particular pitch. In Figure 4b, an adjacent concentric bundle coiling in the opposing direction is added. Finally, in Figure 4c, this pattern is repeated for multiple concentric bundles, showing the type of design for the proposed experimental test sections of this study. The pitch of the coiling bundles relative to each other creates a repeating radial pattern. This

means that based on the pitch of each tube bundle, the interface between adjacent tube bundles changes radially.

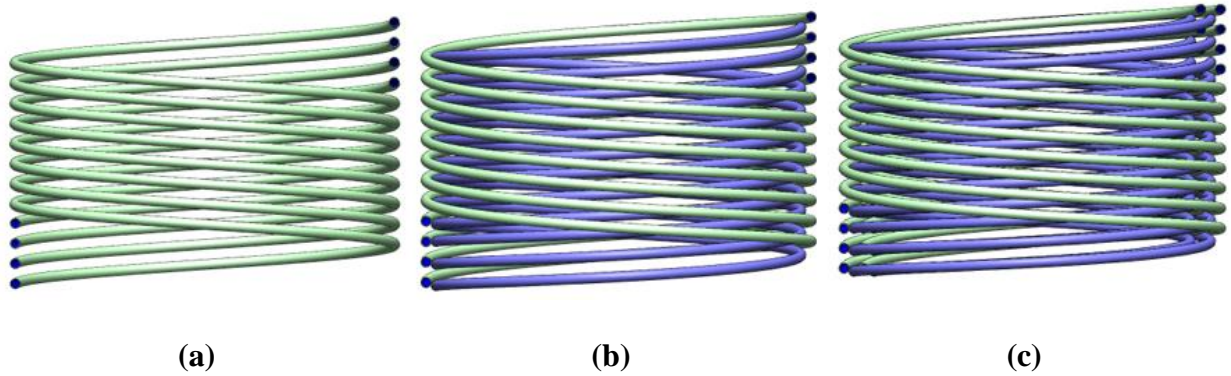


Figure 4 - Design of a helical coil steam generator starting from a) a single helical tube bundle, b) two counter-coiling tube bundles and c) a series of concentric helically coiling tube bundles

This study focuses on a helical coil steam generator design that has five concentric tube bundles in a helical body diameter of 79.5 in or 2.02 m. The helix-to-tube ratio is 127.2. For the first test section, a single interface between two adjacent tube bundles with 12 tubes each was studied. Each of these tube bundles had the same pitch of 16.8 in or 0.43 m for each bundle but they coiled against one another, one with a clockwise and the other with a counter clockwise rotation. Figure 5 demonstrates the coiling behavior and then the interface that was isolated in

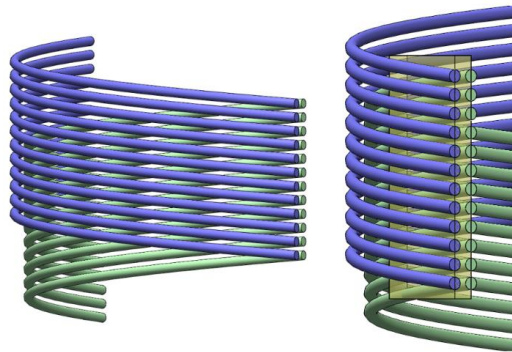


Figure 5 - Design of two inter-coiling tube bundles and region of interest for Test Section I

the test section. The second test section, as seen in Figure 6, used the full design with five concentric tube bundles with side walls. The outer-most and middle tube bundles had 18 tubes and coil with a pitch of 16.8 in or 0.43 m and the two inside tube bundles had 9 tubes and coil with a pitch of -39.2 in or -1.0 m. The length along coils was also different between the two test sections. Test Section I used a 12⁰ section of the entire helical coil body while Test Section II used a 24⁰ section.

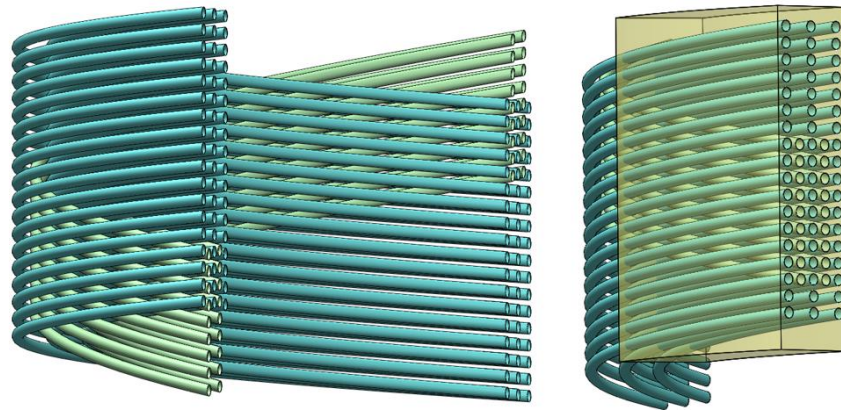


Figure 6 - Design of five inter-coiling tube bundles and region of interest for Test Section II

For many engineering applications, scaling is used when the desired geometry is too large for experimental facility applications. In the case of the helical coil steam generators test sections, no scaling was necessary. The geometry is a one-to-one representation of the heat exchanger with a limit on the radial section of the entire coiling bundle. Due to the purpose of this study, which focuses on the shell-side flow, the tubes used were solid. Therefore, the words tubes and rods will be used interchangeably as one refers to the type of heat exchanger and other, the test sections material.

Both test sections were manufactured out of acrylic in order to enhance the optical clarity when conducting Particle Image Velocimetry (PIV). As both test sections have curved bodies, manufacturing techniques used from the fabricators were crucial to maintaining the index of refraction of the acrylic to that of the fluid used within the test facilities. Drawings for both test sections were created and specified surface finishing to avoid rough surfaces to distort light. For the first test section, half-rods were milled out of solid blocks following a curved body. The two interfaces were then put together using flat side walls to set their distance apart. An acrylic cement that creates a chemical reaction that welds the plastic parts together was used. Figure 7 shows the Computer Aided Drafting (CAD) model for Test Section I and II, where the color of the rods is only meant to show difference in bundles. Test Section II had its own manufacturing challenges which involved the curving of the rod bundles. In order to form the rods to the proper curvature, the manufacturer had to create a mold of the radius and bake the rods onto it. Unfortunately, this practice is very sensitive to the material, heating and cooling procedure. Once the rods were placed into the side walls, the index of refraction had changed. This caused problems later on when capturing PIV frames. Furthermore, the test section was not put together using the same acrylic cement that was used with Test Section II. This also caused issues when running the facility at the necessary flow rate. The adhesive, which had a light brown tint, needed replacement several times during the course of running experiments to avoid leaks through the test section.

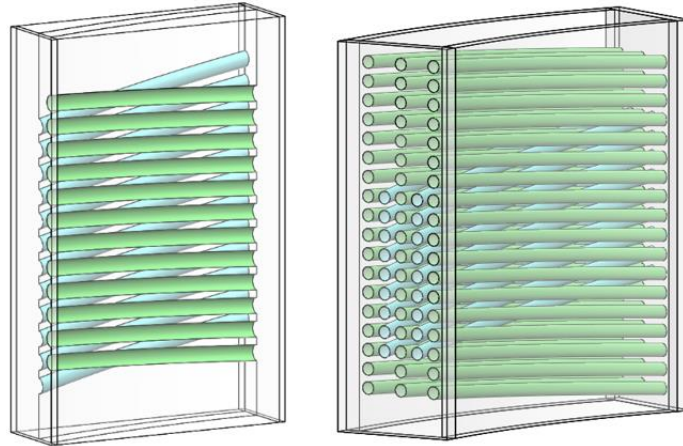


Figure 7 - CAD models of Test Section I and II

In order to have the fluid, p-cymene, move through the test sections, a once-through closed loop was created around the test sections. Both facilities incorporated a tank that connected to a centrifugal pump. The pump was selected to provide enough head to the vertical outlet where a flow meter output the volumetric flow rate of the fluid within vertical pipe. Concerns over the uncertainty of the ultrasonic flowmeter (Krohne OS6300P) lead to validation of the volumetric flow rate using pipes of different materials and fluids and verification of manufacturer accuracy using a pitot tube. The ultrasonic flow meter was determined to have an offset of 3.3% when used with p-cymene and a stainless steel pipe and uncertainty of 1.2%. The pipe lead to a tee junction that divided the flow before coming into an upper plenum. At this tee junction, a thermocouple (OMEGA k-type) was placed to provide temperature readings within 0.2°C . The upper plenum was designed to mix and then condition the flow using honeycombs and screens as described for low speed wind tunnels [27]. Honeycombs were made from PTFE and screens were made from stainless steel in order to avoid deterioration from the hydrocarbon fluid, p-cymene. Figure 8 shows the result of using an adhesive that was silicone based within

the honeycomb – screen assembly with p-cymene after a few experimental runs within Test Section I.



Figure 8 - Honeycomb and screen assembly using silicone adhesive of Test Facility I

After the upper plenum, a reducer and adapter navigated the flow into the test section curved entrance. Each test section was designed to have a fully developed inlet condition. For Test Section I, the pump and entrance effects were determined to be negligible by computational fluid dynamics after the third row of rod interfaces. Test Section II was designed for the fluid to first come through three concentric bundles and then all five further down the test section height. After the test section, the loop was also designed to avoid exit effects by extending the fluid path into the middle of the tank. All parts of the assemblies and the bolts used between them on flanges were stainless steel to avoid any reaction from p-cymene. Gaskets were created from Viton® Fluoroelastomer to prevent leaks in-between the assembly parts. Figure 9 shows both completed Test Section I and II experimental facilities. Table I outlines the characteristic properties of the HCSG design and individual test sections.

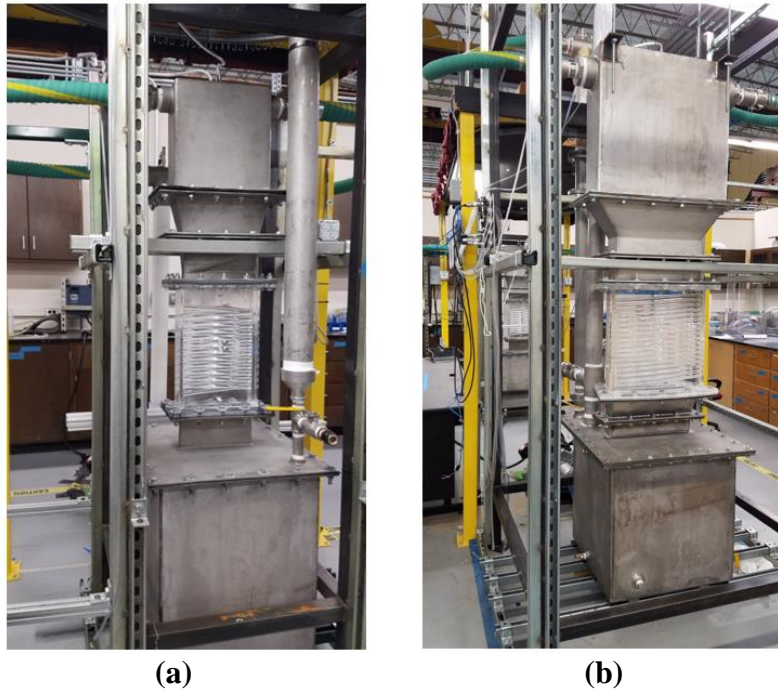


Figure 9 – a) Test Section I and b) Test Section II experimental facilities

Table I. Test Section I and II Design Characteristics

Properties	Test Section I	Test Section II
Helical coil diameter, d_H	2.02 m	2.02 m
Helical pitch(s)	± 0.43 m	+0.43 m, -1.0 m
Central Angle	12°	24°
Rods per bundle	12	18, 9
Rod/tube diameter, d_R	15.9 mm	15.9 mm
Transverse Pitch Ratio, a	2.98	2.98
Lateral Pitch Ratio, b	See Chapter III	See Chapter III

CHAPTER III

EXPERIMENTAL METHOD*

Regions of Interest

As chapter II introduces, the design of HCSG that is used in this study has a constantly changing lateral pitch. This is different to common tube and shell heat exchangers that have a constant cross-section along the helical coils either in-line or staggered tube patterns. Due to the opposing pitches of adjacent tube bundles, this design is very complex and its utilization is limited. Therefore, although it is conducive to higher heat transfer, the fluid behavior is not well studied. In order to study the fluid behavior within the test sections, cross-sectional planes along the z-axis of the test sections were defined in Figure 10. As seen in Figure 10, three Cartesian axes are defined and three planes of interest are shown for each test section. Each plane has a unique lateral pitch ratio that will be defined further in the chapter.

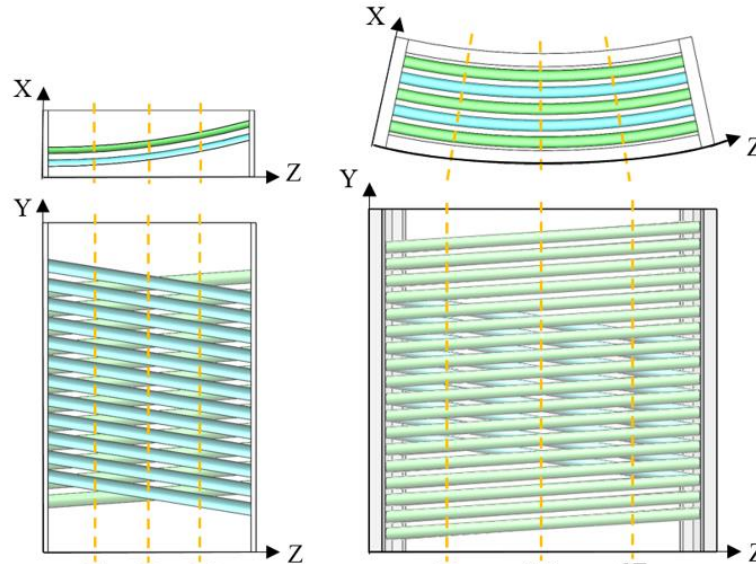


Figure 10 – Test Section I and II with cross-sectional planes of interest

* Reprinted with permission from “Flow visualization study at the interface of alternating pitch tube bundles in a model helical coil steam generator using particle image velocimetry” by Marilyn Delgado, Saya Lee, Yassin Hassan, and N.K Anand, 2018. *International Journal of Heat and Mass Transfer*, 122, 614 – 628, Copyright 2018 by Elsevier.

At each of these planes, the lateral pitch ratio varies. In order to accurately have a representation of the test sections, each test section was scanned at seven cross-sectional planes along the z-axis and reconstructed into CAD models. During this process, images captured along Test Section II appear as seen in Figure 11. An issue is clearly visible marked by the areas in red on Figure 11 where areas of study, below the rods, are not visible to the camera. This is suspected to be a cause of the manufacturing technique that goes into curving acrylic bodies. When heating the rods to curve them, the heating and cooling affects the material properties such as index of refraction. Making the view of the camera, which aims to look through the rod, have a distorted view.

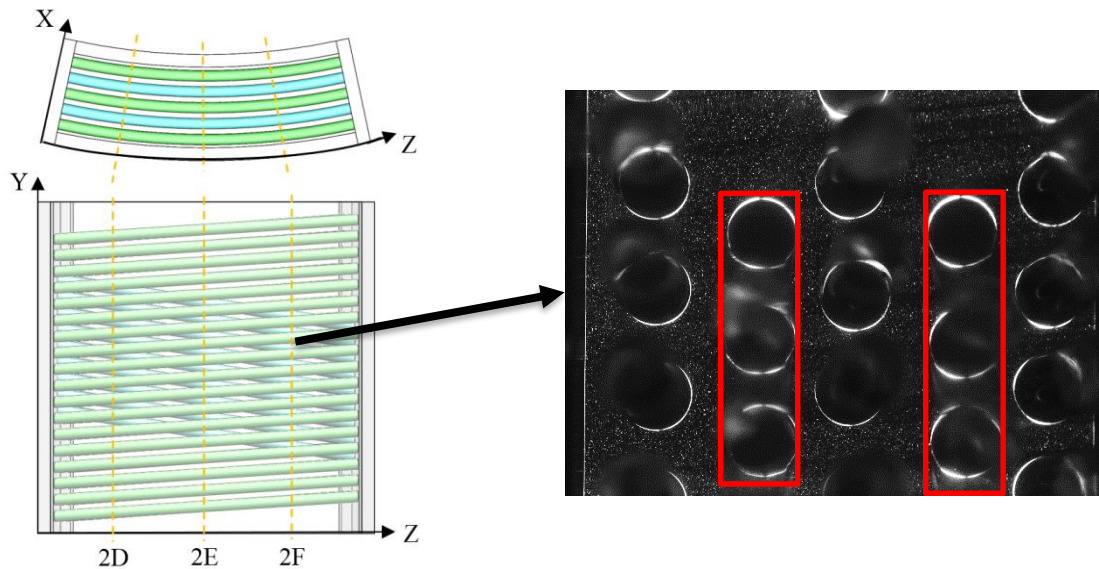


Figure 11 - An example of an image captured in Test Section II with a perpendicular camera and laser set-up

As the study aims to focus on areas of flow between rods in the lateral direction, another method to capture images in order to see below the rods was implemented. The camera and laser

could no longer be perpendicular but at an angle with one another. Optics will show that when a plane and the view angle are not parallel to one another, focus is distorted for everywhere along the plane not parallel. Therefore, to enhance the focus along the plane that is not parallel to the view plane, a Scheimpflug lens was used. Figure 12 demonstrates the new planes that were defined with an angle and the new images captured from the camera view. The camera view results in an image where the flow below the rods is now visible but the image needs to be reconfigured into its original view before analyzed for velocity components.

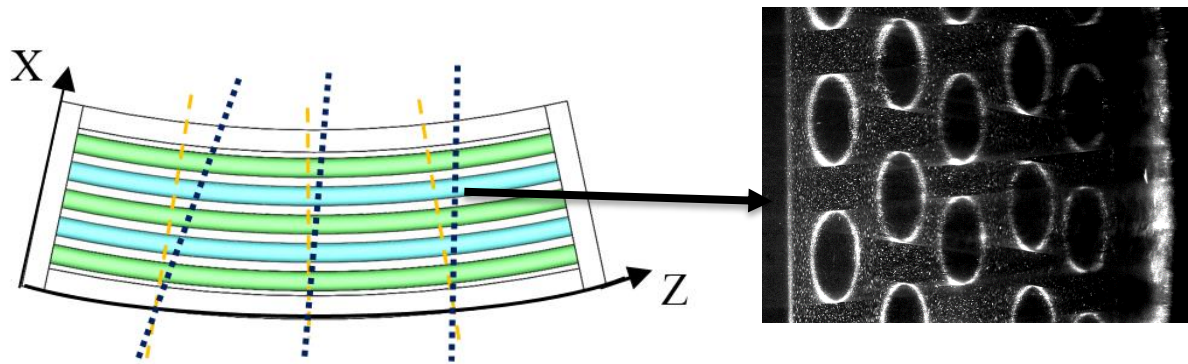


Figure 12 - Test Section II new planes defined for PIV image capture

Particle Image Velocimetry (PIV) Set-up and Method

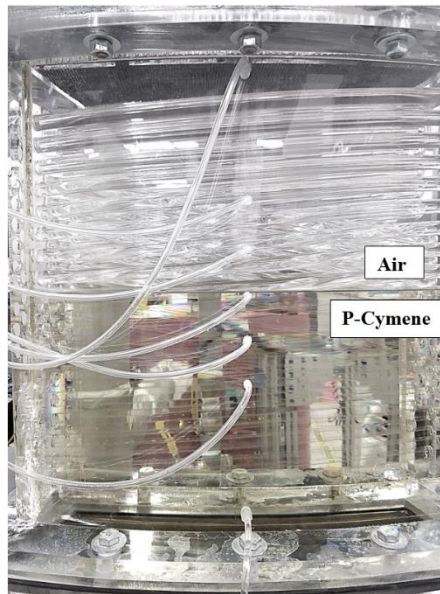


Figure 13 - Test Section II filled with p-cymene and air to demonstrate refractive index matching

High levels of turbulence between rod bundles can be observed through optical velocity flow field measurement techniques such as laser Doppler anemometry and particle image velocimetry, PIV [19]. PIV has become favorable to several techniques because of its ability to capture areas as opposed to individual point measurements. PIV measurements rely on the ability to capture and track the seeded particles in a facility's working fluid to observe flow structure development over time. Both test facilities utilized p-cymene as the working fluid. Studies conducted found that p-cymene and acrylic have the same refractive index at approximately 19°C [28]. Therefore, tests maintained a flow temperature of $21 \pm 1^{\circ}\text{C}$ to maintain indices of refraction between the p-cymene and acrylic similar. An example of this refractive index matching technique is seen in Figure 13.

The settling velocity of the particles must be relatively small compared to the experimental velocity in order for it to be said that the particles follow the flow without

disruption. Stokes number defines how well a particle follows the flow. For this study, silver-coated hollow glass spheres (Potters Industries Conduct-O-Fil® SH400S20) of mean diameter $d_p = 13 \mu\text{m}$ and density $\rho_p = 1.6 \text{ g/cm}^3$ were circulated in Test Section I and Test Section II with a concentration of 60 ppm and 70 ppm, respectively. Stokes number, St , defined by the equation below was calculated to ensure that the ratio of solid response time to fluid response is below 0.01 to say the particle follows the flow without disruption [29].

$$St = \frac{d_p^2 \rho_p V_\infty}{18 \mu d_R} \quad \text{Eq 3.}$$

Equation 3 defines Stokes number where taking the testing temperature window for p-cymene yields a dynamic viscosity $\mu = 0.83 \cdot 10^{-3} \text{ Pa s}$. The inlet velocity, V_∞ , for each test section varied with Test Section I having $V_{\infty 1} = 0.525 \text{ m/s}$ and Test Section II having $V_{\infty 2} = 0.485 \text{ m/s}$. The average Stokes number for the experiments conducted is $5.96 \cdot 10^{-4}$ for $Re = 8,900$ for Test Section I and $5.51 \cdot 10^{-4}$ for $Re = 8,500$ For Test Section II, well below the threshold for uninterrupted fluid flow.

Test Section I PIV Frames

Particles were illuminated by a 532 nm 10 W laser that was focused using optical adjusters to form a 1.5 mm thick laser sheet at each plane. Laser and camera positions were controlled using linear translation stages. In Test Section I, measurements and computational studies showed that entrance effects were negligible after the third adjacent rods; therefore, frames were captured between the fifth and ninth adjacent rod interfaces at planes 1A, 1B and 1C [30]. Multiple areas at the same plane were captured at different heights and compiled together to maintain a higher image resolution and low mm to pixel ratio. A high-speed camera, Photron

Fastcam SA5 1300K-M2, was placed perpendicular to the laser and captured frames at 10,000 frames per second. Each frame captured a window of 896 x 848 pixels, corresponding to a frame size of 24.5 x 23.2 mm based on calibration images. Figure 14 shows the locations and an example of the PIV frame captured at plane 1A. As evident in Figure 14, the laser illuminated particles uniformly unless reflected off the curvature of the rod. These regions were unable to see any particles and therefore, in analysis resulted in no vector areas similar to the areas represented by the half-rods. Depending on the plane, 1A, 1B and 1C, a different magnification factor was used to convert the pixel motion into millimeter velocity components.

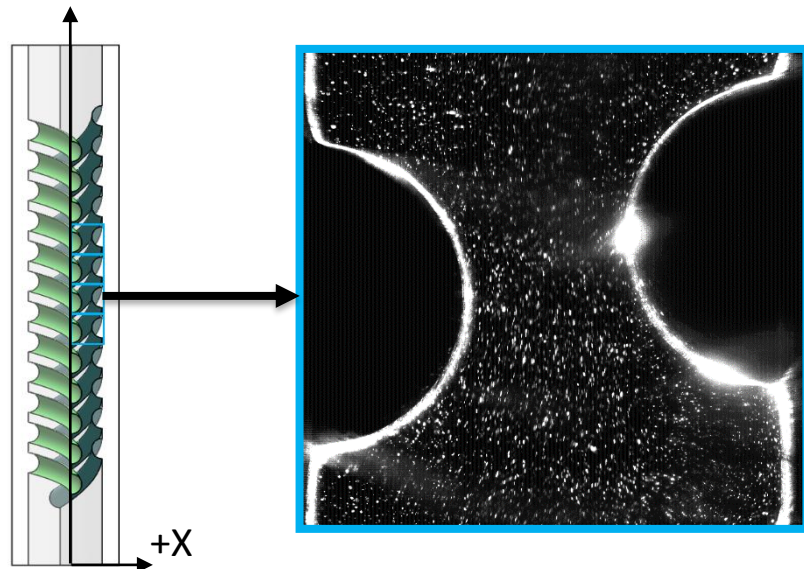


Figure 14 - Test Section I plane 1A and a sample frame

Test Section I PIV Frame Analysis

In order to analyze the frames for velocity components, successive image pairs are analyzed for particle pixel motion. From the image capture rate and a measured length to pixel ratio, velocity can be determined. Using PIVlab, an open source frame analysis code on Matlab,

image pairs were analyzed. PIV techniques rely on the accuracy of the sub-pixel interpolation of the displacement correlation peak to provide an accurate pixel motion measurement. Previous analysis and studies of precision errors suggest that a Gaussian peak-fitting algorithm has the lowest bias and errors [19]. A Gaussian 2x3-point sub-pixel estimator was used with a direct Fourier transform correlation algorithm that included four interrogation area passes and linear window deformation to analyze the frames. A manual frame-by-frame particle tracking method for every 50 from a sum of 1,000 frames for all 12 window areas captured was used to verify the interrogation windows for pixel motion determined by the PIVlab software. The interrogation window sizes were 128x64, 64x32, 32x16, and 16x8 pixels. Additionally, a standard deviation filter was applied to remove vectors that were above the seventh standard deviation. A median filter with the threshold value of 5 and minimum normalization level of 0.1 was applied by post-processing. Due to the change in distance between camera and planes of interest in Test Section I, each plane had a magnification factor determined by the wall to wall length. The average magnification factor for these images was 0.028 mm/pixel.

Test Section II PIV Frames

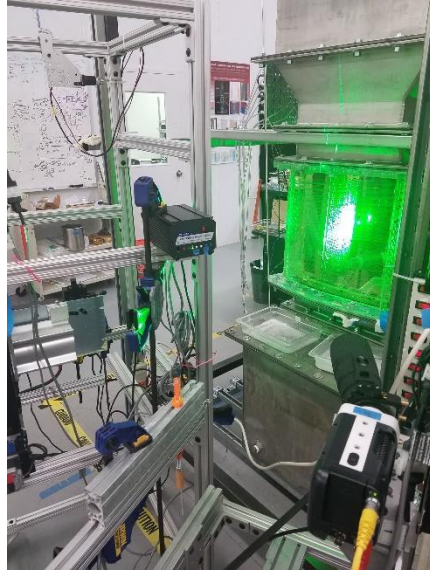


Figure 15 - Scheimpflug Lens Camera and Laser PIV Set-up on Test Section II

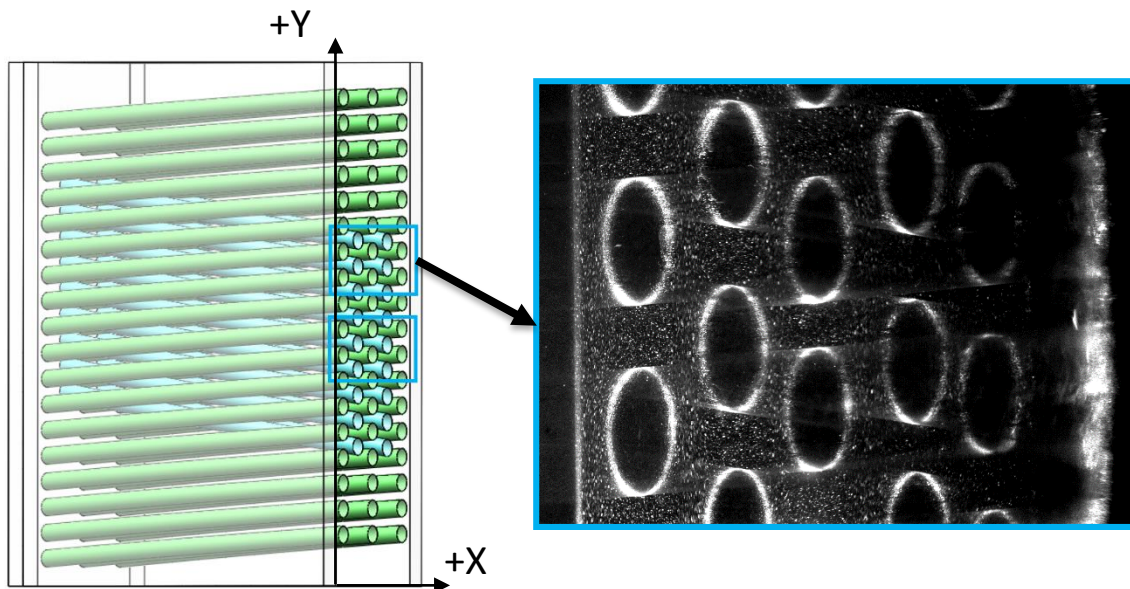


Figure 16 - Test Section II example PIV frame captured using Scheimpflug Lens

Similar to Test Section I, particles were illuminated by a 532 nm 10 W laser that was focused using optical adjusters to form a 1.5 mm thick laser sheet at each plane. Laser and

camera positions were controlled using linear translation stages. In order to capture a plane where particles below the rods were visible, a PIV set-up with the camera and laser not perpendicular to one another was used. Figure 15 shows the camera and laser on the same side of the test section with the Scheimpflug lens attached to the camera. The camera captured an angled view with even focus that is visible in Figure 16. For each angled plane of interest two heights per plane were captured. Previous researchers studied the differences in flow structures between beginning tube rows and those further down the coil bundle. Therefore, the two heights captured for each plane were at the start of all five coil bundles and then at the center of the coil bundle, as shown in Figure 16. A high-speed camera, Phantom MIRO R311, was placed at off-set angles to the laser and captured frames at 4,000 frames per second. Each frame captured a window of 1024 x 768 pixels at an angle precise to the plane of interest.

Test Section II PIV Frame Analysis

The corresponding frame size was determined using the Scheimpflug Lens Principle which accounts for the distortion making the magnification factor no longer constant across the plane. Calibration procedure usually consists of taking images of a flat calibration grid, and then a fit mapping function is computed for each plane [31]. In the case of the image sequences captured across Test Section II, a calibration plate was not used, but instead angles between the plane, camera and test section ends were annotated and used to create a fit mapping factor along the length of the image [32]. Due to the small off-set angles between the laser sheet plane and the perpendicular plane, which were all less than 8° , vertical, y-direction, changes along the x-direction were ignored. This maintained the height of the images at 768 pixels. The images were stretched using a bi-linear interpolation of color depth and were imbedded to ensure the wall to

wall distances fit the scanned models of the test facility. An example of the original image and the corrected image are given in Figure 17. The off-set angles from the original planes of plane 2D', 2E', 2F', and their new dimensions are given in Table II.

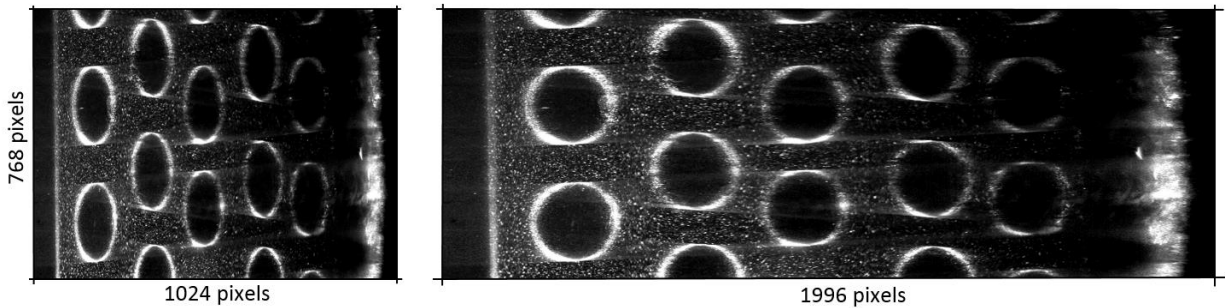


Figure 17 - An original image taken with the Scheimpflug lens and its corrected form

Another noticeable feature of the Scheimpflug lens planes were their unevenly distribution of light across the plane. This is a result from a combination of sources. The reduction in lighting across the plane is a direct result of the angled laser sheet across multiple rod bundles. In Test Section I, the laser sheet was set straight and so the reflection of light off of curved surfaces within the test section were minimal. In test Section II, there are five columns of rods for the light to pass which, as shown in Figure 11 is possible with a perpendicular camera and laser set-up. Unfortunately, the angled laser sheet provides a greater angle for light to reflect off the curved ends of the rods, reducing light that passes through and creating regions of shadows as seen in Figure 17. PIV reliance on particle tracking is dependent on the pixel size of the particle. For most applications, it is good practice to have a particle that occupies a length greater than 2 pixels. Therefore, the image was divided into two areas, the left side where particle size was sufficient and left side where particle size was not large enough. A Gaussian distribution is assumed for the image color scale and brightness was increased by 20% to yield a larger particle size for the right side of the image where illumination was minimized. Unlike Test Section I,

Test Section II has curved walls on the outside of the test section. The change of medium, from acrylic to air, refracts the laser light back into the test section and creates an area of distorted light and shadows. Figure 17 shows this on the far right hand side of the original and corrected images. These areas of light reflection where particles could not be focused are removed before analysis of image pairs through PIVlab.

Table II. Test Section II Corrected Image Properties

Plane	Off-set Angle	Original x-axis length	Adjusted x-axis length
2D'	3.5 ⁰	1024 pixels	1986 pixels
2E'	6.4 ⁰	1024 pixels	1996 pixels
2F'	7.6 ⁰	1024 pixels	2000 pixels

Similar to Test Section I frames, PIVlab was used to perform a cross-correlation of image pairs based on interrogation window sizes. For Test Section II, three interrogation pass step sizes were used, 64 x 32, 32 x 16, and 16 x 8. Similar filters for standard deviation and median threshold were applied in post-processing. From the previous analysis of image adjustment, it is clear that each plane of interest has a unique magnification factor. The average magnification factor for all three planes was 0.066 mm/pixel.

PIV Averaging and Uncertainty

As this study focuses on the average fluid behavior of the velocity components it is worth noting what technique is used to validate this assertion. Similar to way a computational fluid dynamics study uses a sensitivity test to be able to state a convergent solution, a statistical study can be done on the fluid velocity. The more frames used to calculate the mean velocity vector fields, the lower the residual, R , as the root-mean-square (RMS) of the difference between two batches of n and $n-1$ images defined in Equation 4 will be.

$$R_{PIV}^V(n) = \sqrt{\frac{\sum_{i,j=1}^M (V_{i,j}^n - V_{i,j}^{n-1})^2}{N}} \quad \text{Eq 4.}$$

where $V_{i,j}^n$ represents the averaged vertical velocity at (i, j) of the current batch, n , $V_{i,j}^{n-1}$ represents the averaged vertical velocity field at (i, j) of the previous batch, $n-1$, and M is the number of spatial nodes. Three locations of (i, j) were used due to identify different regions of interest. A location at the centerline flow, below the rod and between the two were chosen for their differences in velocity strength. For Test Section I, analysis determined that 5,000 consecutive velocity vector fields corresponding to 1.25 seconds were needed to obtain a statistically steady mean vertical velocity with $R_{PIV}^V < 2\%$. Using the same equation with randomly selected image pairs, an $R_{PIV}^V < 2\%$ was reached with less than 4,000 images for Test Section I. For Test Section II, an $R_{PIV}^V < 2\%$ was reached with 9,500 consecutive images and less than 9,000 images. Statistical results show that random image pairs converge to a lower residual, this is typically seen in flow where eddies are formed and require more image pairs to be resolved in averages [33, 34, 35]. The results presented in Chapter IV for Test Section I are for averages velocity components of 7,000 consecutive image pairs. The results in Chapter V for Test Section II use 10,800 image pairs for average velocity components.

Uncertainty analysis in PIV focuses on a variety of parameters based on instrument and computational uncertainties. Best practice manuals will begin with laser sheet and camera calibration to ensure height and angles of measurement instruments. These calibration uncertainties are typically the largest contributors to PIV uncertainty. Measurement uncertainty can arise from the particle pixel size, number of particles within an interrogation window and magnification factor. A developed study of the factors that affect a PIV system is presented by

Idaho National Lab in 2013 for their matched index of refraction (MIR) facility [36]. A widely used methodology uses uncertainty propagation in the calculation of flow speed, u ,

$$u = \alpha \left(\frac{\Delta X}{\Delta t} \right) + \delta u \quad \text{Eq 5.}$$

where ΔX is the displacement of particle images, Δt is the time interval of successive images, α is the magnification factor identified through the calibration, and δu is an uncertainty factor based on flow image differences such as particle lag or projection uncertainties [32]. For each test section, specific characteristics of the PIV set-up were used. Inlet velocities for each test section $V_{\infty 1} = 525 \text{ mm/s}$ $V_{\infty 2} = 485 \text{ mm/s}$ contributed to the uncertainty in δu and ΔX .

Uncertainty in ΔX is largely from set-up uncertainty which for each Test Section varied. For Test Section I, the maximum distance between the camera and test section plane 1C was based on a perpendicular set up and the frame captured is limited to an area of approximately 25 x 24 mm. Test Section II used a Scheimpflug lens set-up with a larger uncertainty in the angle between the camera and laser that presents itself in ΔX and δu . The distances between the camera and laser also vary with a larger range than the Test Section I set-up. The largest distance between the camera and laser in Test Section II is to plane 2D'. The largest angle off-set from a perpendicular set-up was plane 2F', with a reconstructed plane with length in the x-direction of 2000 pixels. This reconstruction created an uncertainty in magnification in the x-direction that was larger than the uncertainty in the y-direction, and was therefore used to determine total maximum uncertainty for Test Section II. Magnitude for the uncertainty of each parameter in flow speed calculation for both test sections is given in Table III.

Table III. Uncertainty Properties for Test Section I and II

Error sources	TSI Uncertainties	TSII Uncertainties
Magnification factor, α	0.028 mm/pix	0.066 mm/pix
Image displacement, ΔX	12.50 mm/s	25.6 mm/s
Image interval, Δt	0.02 mm/s	0.02 mm/s
Experiment, δu	0.80 mm/s	1.33 mm/s
Combined uncertainty of PIV, $\sigma_{C,PIV}$	17.87 (mm/s)	29.2 (mm/s)

CHAPTER IV

TEST SECTION I RESULTS *

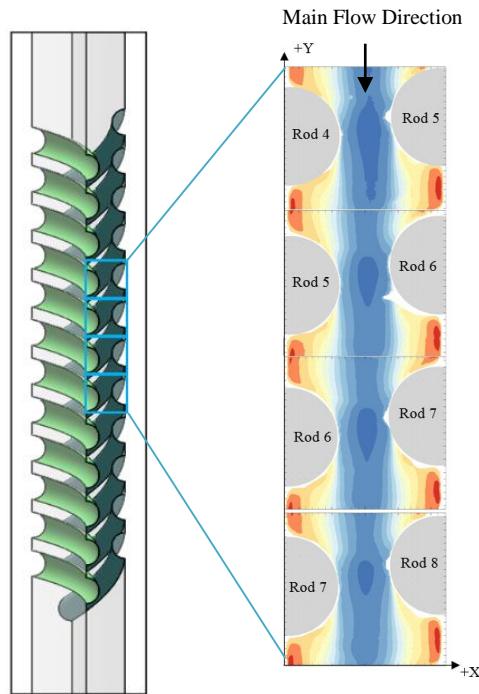


Figure 18 - Test Section I plane and the 4 frame areas. Across each of the three planes, four frame heights were taken for a total of 12 frames in Test Section I for average velocity fields

Across the three planes of interest in Test Section I, 1A, 1B, and 1C, three frame windows per plane were taken for a total of twelve frames. PIV analysis and averaging for 7,000 frames was conducted for each of these frame areas, each capturing a window of 896 x 848 pixels, corresponding to a frame size of 24.5 x 23.2 mm. Figure 18 presents plane 1A and the four heights captured along the plane in the y-direction. Due to the changing geometry at each

* Reprinted with permission from “Flow visualization study at the interface of alternating pitch tube bundles in a model helical coil steam generator using particle image velocimetry” by Marilyn Delgado, Saya Lee, Yassin Hassan, and N.K Anand, 2018. *International Journal of Heat and Mass Transfer*, 122, 614 – 628, Copyright 2018 by Elsevier.

plane, fluid properties will be discussed with relation to the rod row and not on location along the x-and y-axes.

Cross-flow on the shell side of a tube and shell heat exchanger is characterized most typically by two regions. Streamline flow is high velocity flow between the rods that follows the main flow direction. Wake region flow is characterized by eddies that form below the rods. These regions are best shown in Figure 19 which shows an example frame taken at plane 1C. Experimental and numerical studies have shown that the vortex formation below the rods can be symmetric or alternating, and are also susceptible to wake switching and shedding based on the geometry of the tube arrangement [19, 21, 26]. The formation, strength and development of these vortices are topics for study when discussing potential risk from flow induced vibration [24, 25].

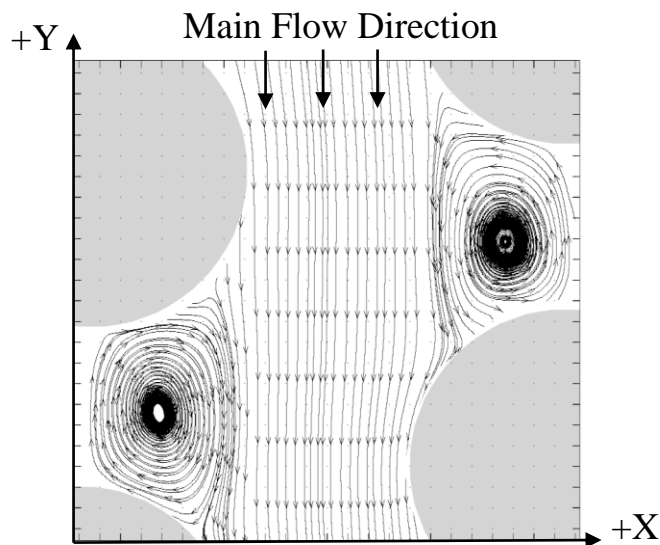


Figure 19 - Crossflow fluid structures within Test Section I

At each of the planes of interest, the lateral pitch ratio differs as is evident in Figure 20. Vortex behavior is commonly associated with the lateral and transverse pitch ratio of the tube bundle. The geometry in this study makes it unique in comparison to the various studies that use constant tube arrangements, most commonly inline and staggered. The experimental average

velocity components can be looked at individually per plane for their respective lateral pitch ratio.

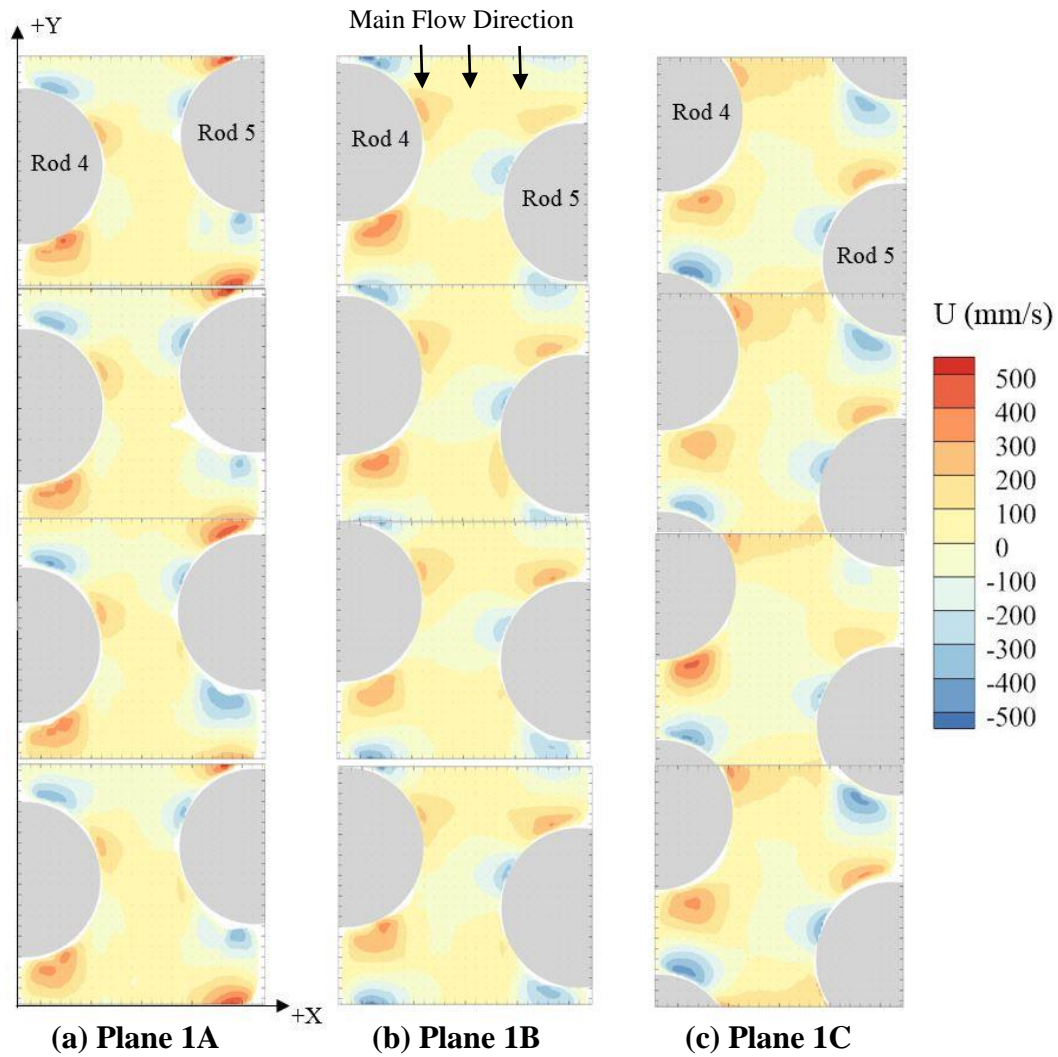


Figure 20 - Velocity in the x-direction, U (mm/s), for Test Section I planes

Figure 20 presents the x-direction or transverse velocity, U (mm/s), for the four frame heights across the three planes of interest. The areas in white represent areas where light reflection prevented particles from being visualized and grey areas represent a pseudo rod location, due to the differences in machined acrylic and perfectly circular geometry. Evident across all three planes is the lack of strong negative or positive flow in the x-direction in the

streamline region between the rods. This is expected behavior of cross flow over tube bundles. The lateral pitch ratios for the Test Section I planes are 0.20, 0.39 and 0.91 for planes 1A, 1B and 1C, respectively where the bundle on the left hand side is coiling upward and the right side bundle is coiling downward from plane 1A to 1C. From Figure 20 it is evident that the recirculation region strengths vary between plane and rod row. The inlet velocity for Test Section I, $V_{\infty 1} = 525$ mm/s, is approximately the magnitude of the recirculation region velocity maximum and minimum for plane 1B and 1C. Plane 1A's geometry is closest to an inline tube bundle arrangement, with $b_{1A} = 0.20$, and shows the highest transverse velocity below all rod rows. For planes 1B and 1C, the recirculation regions below the rods are weaker in transverse velocity compared to plane 1A but also show a pattern in rod row. In plane 1B, the recirculation region strength decreases as the rod row increases; The opposite is seen in plane 1C. The recirculation direction is very consistent across the three planes, which can be attributed to the close wall. In a typical staggered tube bundle, vortices form and commonly switch direction below the rods. In this test section, the vortex that forms below the rod is limited by the wall and physically cannot exhibit the same behavior. A summary of the average x-direction velocity components and their respective planes is given in Table IV.

Table IV. Characteristic x-direction velocity, U (mm/s), for Test Section I

Plane	b	U _{MAX} (mm/s)	U _{MIN} (mm/s)
1A	0.20	717.72	-405.71
1B	0.39	379.32	-503.81
1C	0.91	429.99	-508.88

The lateral velocity, V (mm/s), of the three planes for Test Section I is seen in Figure 21. The lateral velocity follows the main flow direction and across each plane, this velocity is approximately three times the inlet velocity of the test section, $V_{\infty 1} = 525$ mm/s. Similar to the

velocity in the transverse direction, there are patterns visible within and across each plane for the lateral velocity component. The region below the rod indicates the lateral velocity strength of these recirculation regions. In plane 1A, the highest vertical velocity is seen throughout the plane to be below the right side bundle. This is the opposite in plane 1B, where the left side bundle has the higher positive lateral velocity. For plane 1C, this vertical velocity below the rod shows no consistent behavior in regards to rod bundle or rod row.

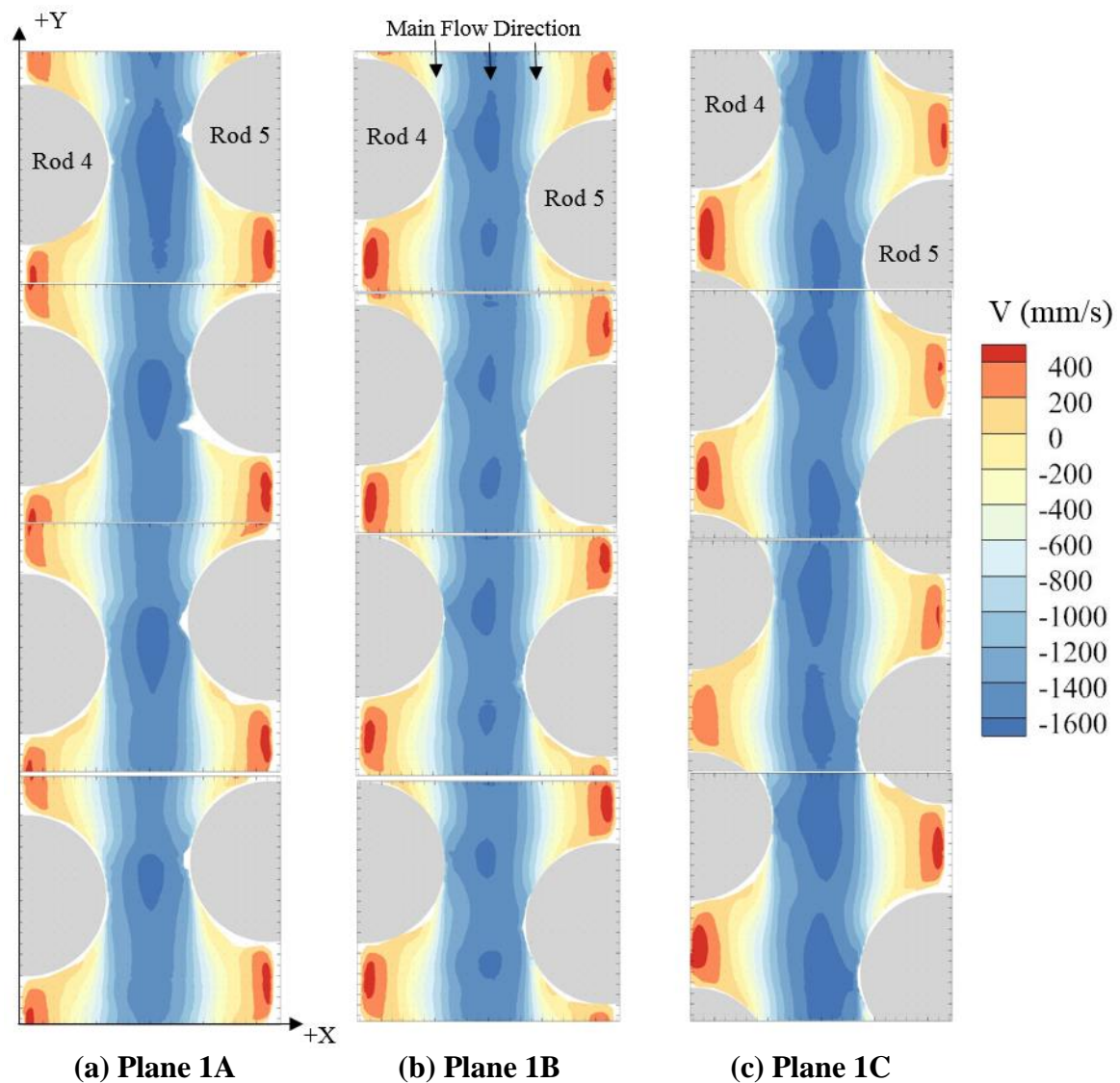


Figure 21 - Velocity in the y-direction, V (mm/s), for Test Section I planes

From Figure 21, it is also visible that the streamline between the rods shows a consistent behavior throughout each plane. In plane 1A and 1C, the streamline flow is consistently highest at the narrowest point between the two adjacent bundles. This follows from standard fluid mechanics without regard for the fluid behavior in the z-direction. In plane 1B, the region of highest vertical velocity consistently aligns beside the wake. This average fluid behavior suggests the development and slipping of vortices from below the rods to the center streamline. A summary of the average y-direction velocity components and their respective planes is given in Table V. Outside of velocity components, streamline, vorticity, and Reynolds stresses were taken from the PIV frames and summarized [37].

Table V. Characteristic y-direction velocity, V (mm/s), for Test Section I

Plane	b	V_{MAX} (mm/s)	V_{MIN} (mm/s)
1A	0.20	535.90	-1765.1
1B	0.39	571.94	-1665.7
1C	0.91	581.38	-1717.2

CHAPTER V

TEST SECTION II RESULTS

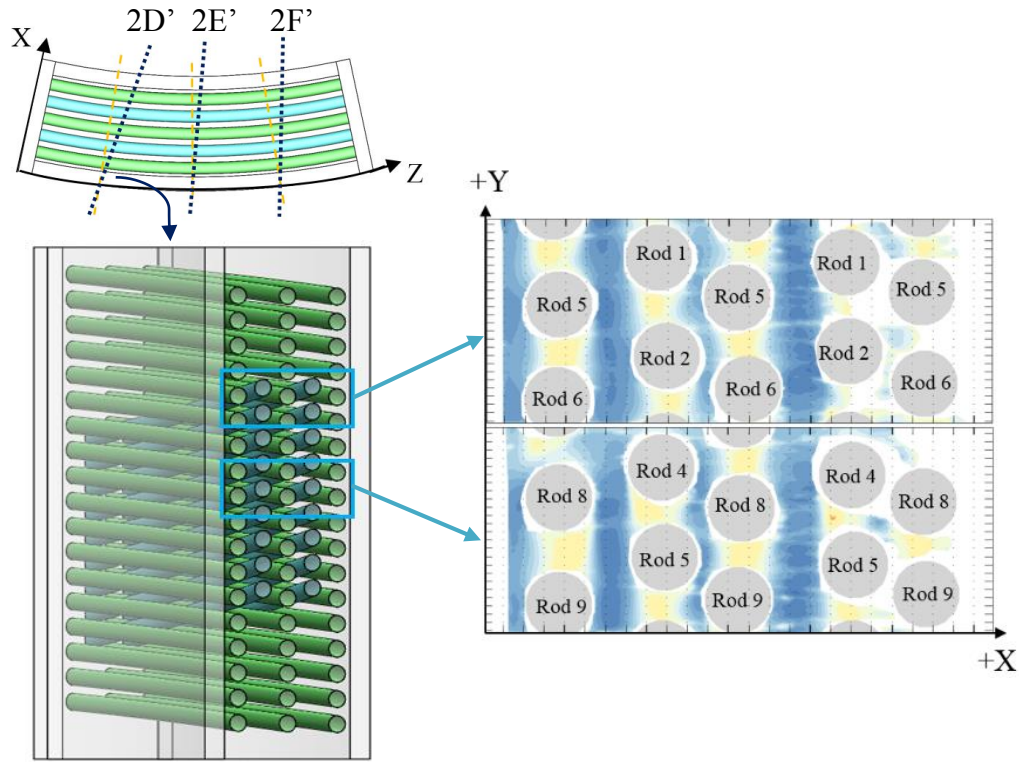


Figure 22 - Test Section II planes and the 2 frame areas. Across each of the three planes, two frame heights were taken for a total of 6 frames in Test Section II

Similar to Test Section I, the frame areas for Test Section II are shown in Figure 22. Two heights per plane were looked at to study the fluid behavior at the start of all five rod bundles and then at the center. Similar flow visualization studies have shown that fluid behavior at the first and center rows exhibit different recirculation region behavior [19,20,21]. Therefore, as Figure 22 presents, the rod row of the second and fourth bundles mark the height at which the frame was taken. Test Section II has similar flow behavior to Test Section I, in that the fluid structures are divided into two main regions, the streamline between the rods and the wake regions below the rods. In Test Section II, rods are fully circular in a 2-D cross-section and flow can move

between the five rod bundles. An example of the instantaneous cross-flow behavior that is witnessed in the PIV frames is seen in Figure 23. Figure 23 presents an instantaneous streamline plot from Test Section II at plane 2F'. From the figure it is clear that the streamline flow does not follow the main flow as uniformly as it did in Figure 19 for Test Section I. This is evident from the vortices that have developed below the rods and are also seen in or entering the streamline.

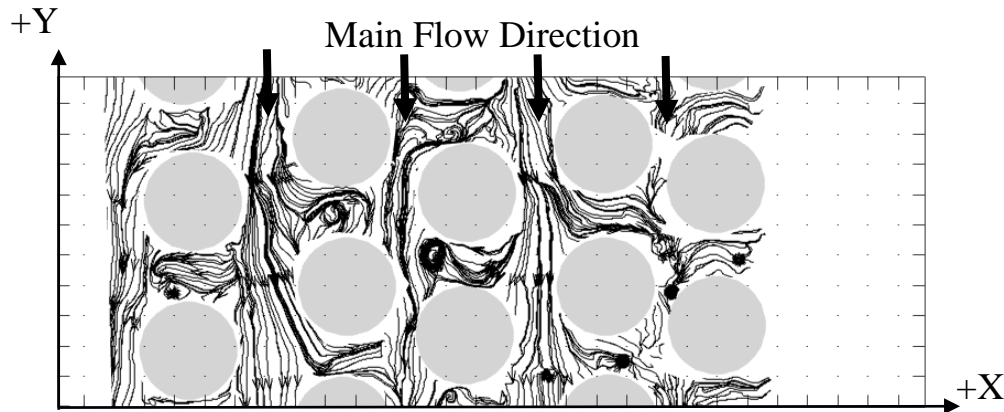


Figure 23 - Cross-flow fluid structures within Test Section II

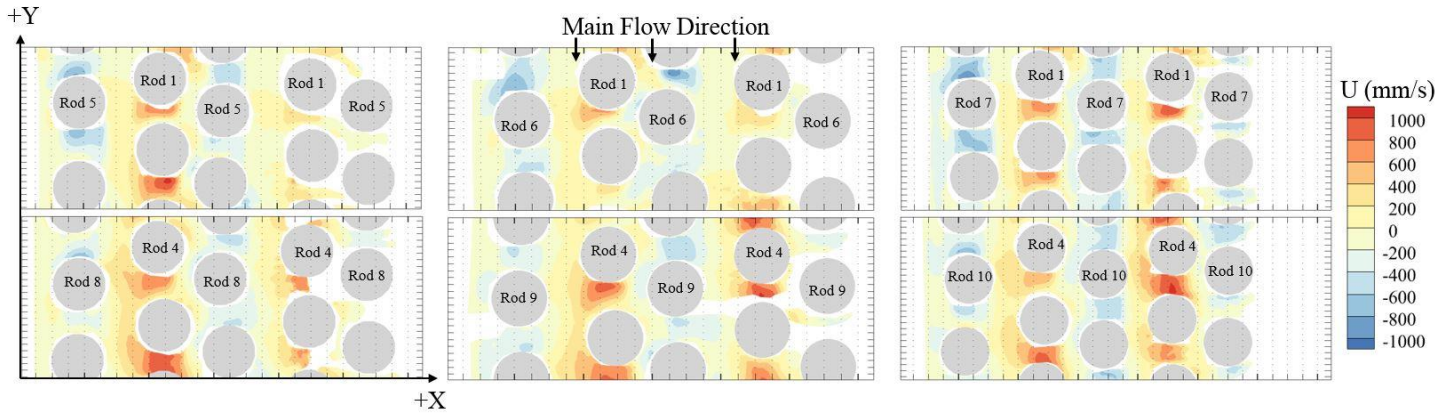
At each plane of interest, the transverse pitch ratio remains the same while the lateral pitch ratio changes. From Figure 23, it can be seen that the bundles do not have a uniform lateral pitch ratio. The manufacturing process of bending and fitting concentric tube bundles using a plastic like acrylic created this large tolerance. Table VI shows the average lateral pitch ratio, \bar{b} , defined for each plane and the respective standard deviation, σ_b , for a sample of sixteen lateral pitch ratios within the plane.

Table VI. Test Section II average lateral pitch ratio and standard deviations per plane

Plane	\bar{b}	σ_b
2D'	0.75	0.12
2E'	0.60	0.15
2F'	0.81	0.15

Figure 24 shows the average x-direction velocity, U (mm/s) for Test Section II planes with an inlet velocity of $V_{\infty 2} = 485$ mm/s. A noticeable difference between the frames captured in Test Section I and II is seen in Figure 24. The frames captured per plane were not taken across the same height. This is identified by the rod row labeled across each plane. From plane 2D' to 2F', the first, center and last rod bundles are coiling upward, while the second and fourth bundle coil downward.

Figure 24 illustrates the transverse velocity component of the flow across the three planes. Due to the light reflection and manufacturing tolerances, the areas in white represent regions where the particles were not visible and analysis was not done. The regions in grey represent a pseudo-rod position. Average velocity behavior can be seen divided into the two regions typical of cross flow, the streamline and wake regions. Streamline flow in the transverse direction is very minimal. Transverse flow in the wake regions below the rods show fluid behavior similar to staggered tube bundle arrangements [19,21]. Across all three planes, the transverse velocity changes strength dependent on the rod bundle. The wake regions below the rods in the first, center and last rod bundles show a negative velocity strength about -1000 mm/s or twice the inlet velocity. The wake regions below the rods in remaining rod bundles show a positive velocity strength about -1000 mm/s. Although it is typical for transverse flow to be twice the strength of the inlet velocity in cross-flow, the change in direction is a characteristic specific to staggered tube bundle arrangements with larger lateral pitch ratios [21]. This phenomenon in transient flow is called alternating vortices and are common of the Coanda effect, or wake switching [21, 26] when they occur behind rods of the same bundle.



(a) Plane 2D' (b) Plane 2E' (c) Plane 2F'
Figure 24 - Velocity in the x-direction, U (mm/s), for Test Section II planes

The strength of the transverse velocity between the first rod rows and the center vary depending on the plane. In all three planes, Figure 24 shows that the transverse velocity behind the second and fourth rod bundles increases as the rod row increases. The opposite is seen for the transverse velocity behind the first, center and last rod bundles. The negative transverse velocity below these rods decreases as the rod rows increase. Another notable feature characteristic of alternating vortices behind rod rows is the location of the maximum velocity in the wake regions. Not only does the flow direction change between rod bundles, but the location of the highest velocity also switches between rod bundles. An example of this behavior is seen in plane 2F' across the first rod row. Characteristic transverse velocity components for each plane is given in Table VII.

Table VII. Characteristic x-direction velocity, U (mm/s), for Test Section II

Plane	b	U_{MAX} (mm/s)	U_{MIN} (mm/s)
2D'	0.75	1047.6	-877.2
2E'	0.60	1202.7	-919.46
2F'	0.81	965.22	-1073.1

Figure 25 shows the results of the average vertical velocity, V (mm/s), across the three planes of Test Section II for the two heights of interest. The velocity in the vertical direction is mainly characterized by the streamline flow between the rod bundles. As previously mentioned, the high tolerance in manufacturing influenced the design of the test section and some fluid behavior can be seen as a result. The area between the third and fourth rod bundles is not uniform to the surrounding tube bundles in planes 2D' and 2E'. This can be categorized as a change in transverse pitch that in plane 2F' changes itself to a more uniform pitch in the rod curvature. The influence it has is evident in the vertical velocity within that region. For all planes, the vertical velocity with the highest magnitude is the streamline velocity between the third and fourth rod bundles accounting for the areas where the transverse pitch is narrower. A notable fluid behavior is the vertical velocity in the wake regions. From Figure 24, it can also be seen that the average vertical velocity below the rods focuses on a small region to one side of the rod. Comparing Figure 24 and 25, the highest vertical velocity region matches the highest transverse velocity below the rods. The positive vertical velocity is indicative of vortices forming and the consistency in area is suggestive as well for alternating vortices between rod rows [21, 26]. Vertical velocity within the wake regions do not show any consistent pattern across rod rows or rod bundles. This is typical of staggered and inline tube bundles [19, 20, 21]. Characteristic transverse velocity components for each plane is given in Table VIII.

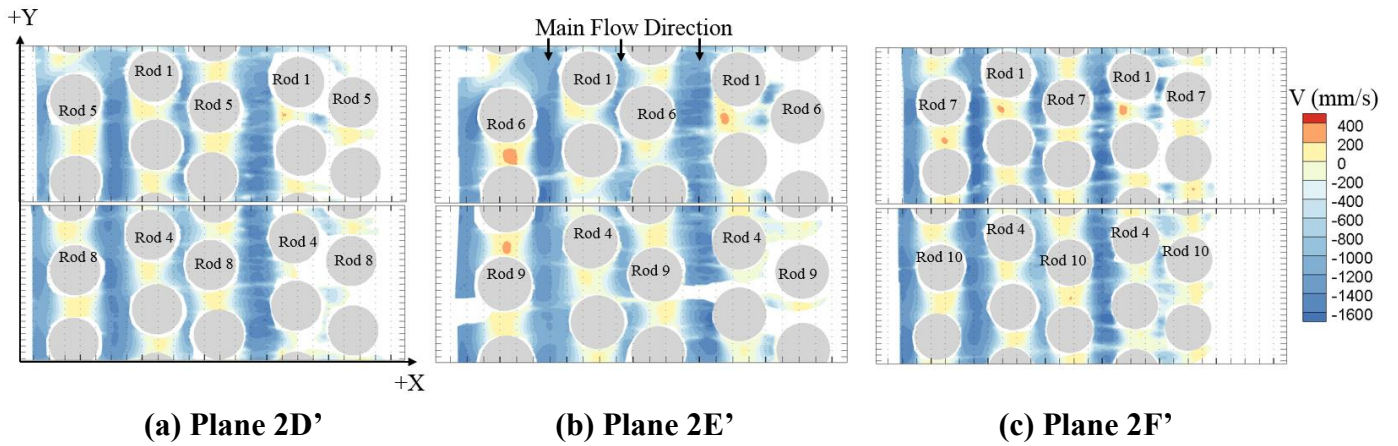


Table VIII. Characteristic y-direction velocity, V (mm/s), for Test Section II

Plane	\bar{b}	V_{MAX} (mm/s)	V_{MIN} (mm/s)
2D'	0.75	320.2	-1874.4
2E'	0.60	288.44	-1786.7
2F'	0.81	205.47	-1786.4

CHAPTER VI

DISCUSSION AND CONCLUSIONS

Comparison and Discussion

Velocity components in the transverse and lateral direction were presented for Test Section I and Test Section II in Chapters IV and V, respectively. Using the inlet velocity for each test section to calculate Reynolds number using the characteristic length of rod diameter, common of tube and shell heat exchangers, a comparative study between normalized velocity and lateral pitch ratio is presented. Test Section I, with inlet velocity $V_{\infty 1} = 525$ mm/s had a Reynolds number 8835 and Test Section II inlet velocity, $V_{\infty 2} = 485$ mm/s had a Reynolds number 8445. A summary of the lateral pitch ratio across all the planes in Test Sections I and II is given in Table IX.

Table IX. Lateral Pitch Ratio, b, for each plane across Test Section I and II

Plane	b
1A	0.20
1B	0.39
1C	0.91
2D'	0.75
2E'	0.60
2F'	0.81

In order to look at the velocity components compared to the lateral pitch ratio, velocity components were normalized using the following equation,

$$U_n = \frac{|u_{max/min}|}{V_{\infty}} \quad \text{Eq 6.}$$

Figure 26 presents the normalized velocity components as a function of lateral pitch ratio for each velocity component.

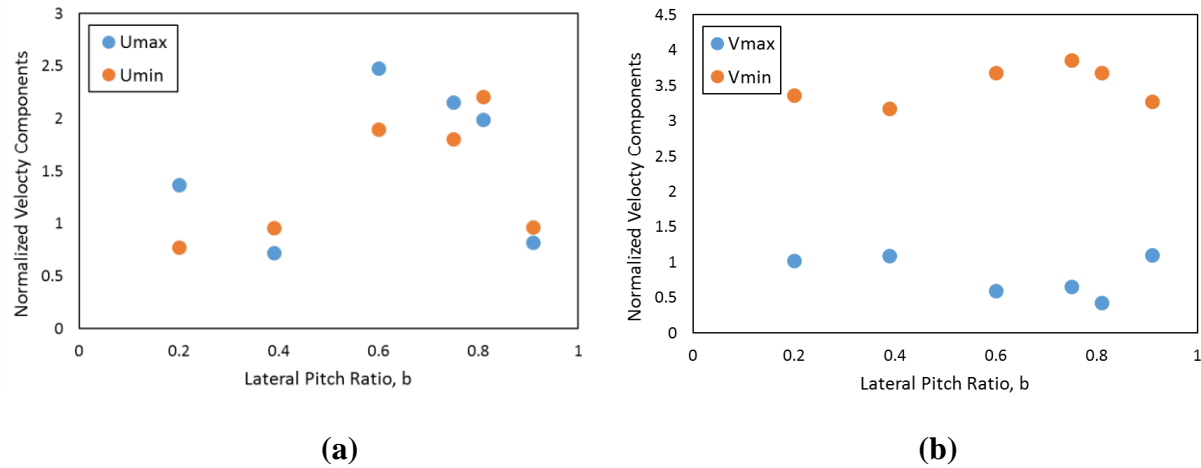


Figure 26 – Extrema as a function of Lateral Pitch Ratio for (a) transverse and (b) vertical velocity components

In a typical staggered tube bundle, the lateral pitch ratio is closely related to the transverse velocity as it dictates the space between off-set adjacent tube bundles and creates narrower areas for shell side flow to move through [6, 11, 13, 14, 18, 19, 20]. An initial look at that influence is from the extrema transverse velocity components. From Figure 26, there is no clear relationship between the lateral pitch ratio and any of the normalized velocity components. The transverse velocity components in Figure 26a show a pattern that appears related to the test section rather than lateral pitch ratio. Figure 27 looks at the transverse velocity extrema as a function of lateral pitch ratio for Test Section I and II separately.

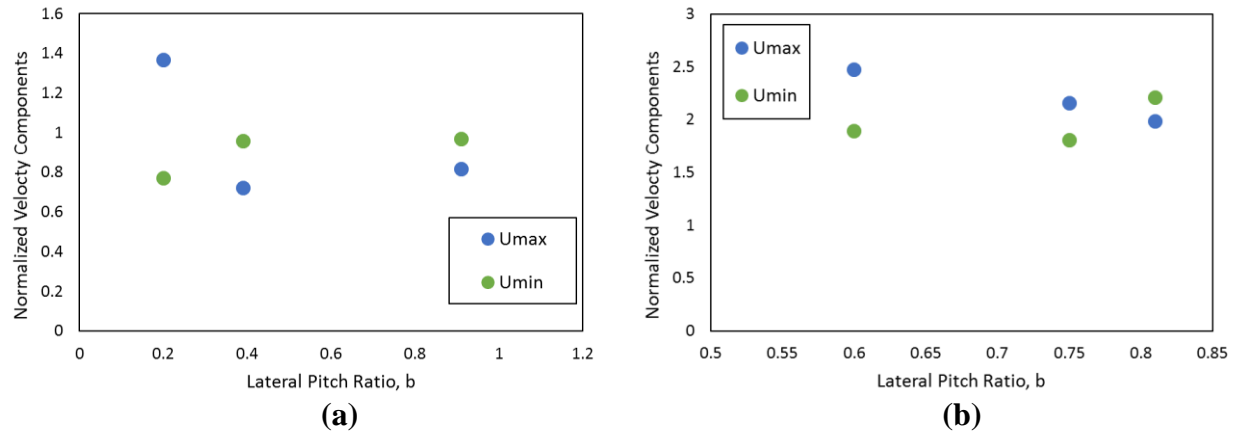


Figure 27 – Normalized maximum and minimum transverse velocity as a function of Lateral Pitch Ratio for (a) Test Section I and (b) Test Section II

The maximum transverse velocity in both Test Section I and II decreases as lateral pitch ratio increases, opposite of a typical staggered tube bundle. The minimum transverse velocity is commonly found within the streamline flow and therefore, as the lateral pitch ratio increases, studies have shown this to also increase the vortex shedding behavior [14, 16, 19]. From Figure 27, the typical pattern of increased transverse velocity to a larger lateral pitch ratio is visible in only in the minimum velocity in Test Section I and II. Maximum transverse velocities decrease as lateral pitch ratio increases.

A more comprehensive comparison between the two helical coil steam generator test sections is by looking at the two main flow areas individually, similar to previous researchers [14, 19, 20]. As mentioned previously, the flow is divided into a streamline flow that follows the inlet flow direction, and the flow between the rods in the wake region. Test Section I and II both have a fifth rod row that at each plane has a unique lateral pitch ratio, b . At this fifth rod row, flow velocity components can be divided by region, streamline or wake flow velocity intensity. Figure 28 illustrates the wake and streamline regions using an example frame from Test Section

I. Using the same normalization from Equation 6, Table X compares the average streamline and wake velocity intensity for both test sections across the fifth rod row.

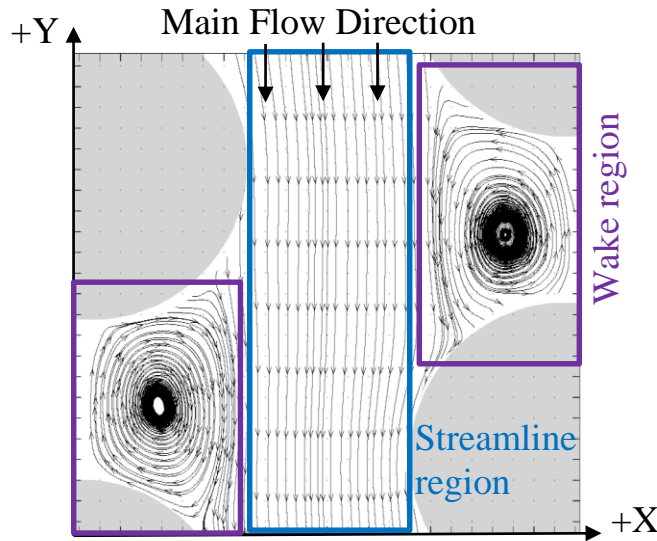


Figure 28 – An example of the wake and streamline regions within the planes of interest in Test Section I and II

Table X. Streamline and wake velocity intensity for the fifth rod row in TS I and II

Plane	b	$U_{N,W}$	$V_{N,W}$	$U_{N,ST}$	$V_{N,ST}$
1A	0.2	0.18	0.59	0.07	2.79
1B	0.39	0.21	0.67	0.08	2.69
1C	0.91	0.23	0.70	0.11	2.77
2D'	0.75	0.53	0.31	0.20	2.31
2E'	0.6	0.58	0.38	0.32	2.30
2F'	0.81	0.61	0.44	0.25	2.53

A study conducted by Paul, Tachie and Ormiston [19] conducted particle image velocimetry measurements within a staggered tube bundle arrangement, of rod diameter 2.54 cm, with transverse and lateral pitch ratios of 3.8 and 2.1, respectively at a Reynolds number of 9300. Similarly, they determined several rod row height vertical and transverse velocity intensities. The geometry of the tube bundle, as seen from the difference in transverse and lateral pitch ratio, has much larger regions between the tubes. In a bundle arrangement that is closer together with transverse pitch ratio of 2.98 and lateral pitch ratios no greater than 1, such as the design of heat

exchanger in this study, the recirculation regions are limited by the lateral pitch ratio.

Nevertheless, in comparing average velocity components, vortex development and motion within the bundle is not compared.

Streamline vertical velocity intensity, $V_{N,ST}$, within the present study's design ranged from 2.3 to 2.8. The determined streamline vertical velocity within the study from Paul et al. averaged at 1.75, showing good agreement between a more compact design and a higher velocity. Nevertheless, the streamline transverse velocity intensity, $U_{N,ST}$, in the present study differs between test sections, where for Test Section I the average is around 0.08 and for Test Section II it is averaged at 0.25. The average streamline transverse velocity intensity of the study from Paul is averaged at 0.20. Vertical velocity within the streamline is less dependent on the tube bundle than the transverse velocity [14, 19, 20]. At a similar Reynolds number and the same rod row within the bundle, the effect of the transverse and lateral pitch ratios are evident. The bundle arrangement within the study by Paul et al. [19] has a much larger transverse and lateral pitch ratio than the one presented in this study. This is especially evident when looking to compare wake region velocities. Due to the large lateral pitch ratio, the behavior of the flow behind the rods differs. Within the design in this study, the vortices form to the height of the lateral pitch. Within the flow visualization study of Paul et al. [19] the lateral pitch is many times larger than the diameter of the rod that symmetric vortices form behind the rod and streamline flow follows into the wake until the next rod interrupts the flow. This phenomenon is not visible at any time within the two test sections of the present study.

Between the planes of their respective test sections, the average streamwise and wake velocity components can be compared. From Table X, all velocity components in the streamwise and wake region increase across planes 1A, 1B and 1C with increasing lateral pitch ratio. Unlike

the previous extrema measurements presented, this is consistent with expected fluid behavior in tube bundles. Planes 2D', 2E' and 2F' from Test Section II do not show the same pattern. The average velocity component behavior does not change uniformly with or against the lateral pitch ratio. The inconsistency between Test Section I and II suggests a difference in the fluid behavior which cannot be directly attributed to the lateral pitch ratio.

Conclusions

Shell side fluid behavior across two helical coil steam generators were studied. Test Section I simplified the geometry to an interface between two inter-coiling bundles. Test Section II expanded the geometry to five concentric bundles with adjacent rod bundles coiling against one another with different helical pitches. Each test section had a constant transverse pitch ratio of 2.98 and changing lateral pitch ratio that varied along the bundle geometry. Three planes across each test section, with unique lateral pitch ratios, were studied using particle image velocimetry at a Reynolds number of approximately 8,500. Average velocity fields were determined for the transverse, x-direction, and vertical, y-direction, components. The results for each test section were presented and showed the development of two main flow regions, the streamline flow between rod bundles and the wake flow behind rods. Streamline flow characteristics showed agreement with previous studies conducted with staggered tube bundle arrangements where the increase in lateral pitch ratio increases the velocity strength for Test Section I [14, 19, 20, 21]. Average wake velocity components in both test sections showed an alternating behavior behind the rods suggesting vortex shedding cycles behind the rods [14, 21]. The wake regions behind the rods of Test Section I do not show a pattern that can be directly related to the change in lateral pitch ratio. The relative location along the coil provided a better

physical explanation of the velocity magnitudes seen across all three planes in Test Section I. The simplification of heat exchanger design for Test Section I can also be considered to impose wall effects not visible in Test Section II. The velocity in the wake regions of Test Section II suggest that the vortices form non-symmetrically behind the rod. The direction of the vortex also switches every adjacent rod bundle. This behavior is also suggestive of wake switching or the Coanda effect as observed by previous studies in staggered tube bundle arrangements [21, 26].

A study to examine the fluid structures between helical coil steam generators was conducted and showed strong agreement for the development of vortex shedding cycles behind rod bundles. Averaged velocity measurements did not show strong support between lateral pitch ratio and patterns in velocity magnitude. The average velocity fields suggest that relative location along the coiling bundle also contributes to the velocity magnitudes of the wake regions below the rods. In order to characterize the wake region fluid behavior, future work aims to study the transient behavior of the flow to have an in-depth analysis of the relationship between lateral pitch, transverse pitch, radial location around the helical coil tube bundle and recirculation region development.

REFERENCES

1. D.G. Prabhanjan, V.G.S. Raghavan, and T.J. Rennie, "Comparison of heat transfer rates between a straight tube heat exchanger and a helically coiled heat exchanger," *Int. Communications in Heat and Mass Transfer*, **29**(2), pp.185 (2002).
2. IAEA, *Innovative Small and Medium Sized Reactors: Design Features, Safety Approaches and R&D Trends*, Tech. Rep. IAEA-TECDOC-1451, International Atomic Energy Agency, Vienna Austria (2005).
3. N.V. Hoffer, N.A. Anderson, and P. Sabharwall, "Development and Transient Analysis of a Helical-coil Steam Generator for High Temperature Reactors," *Journal of Young Investigators*, **22** (2), pp. 40-50 (2011).
4. E.K. Kim, and S.O. Kim, "Sodium-Cooled Fast Reactor Helical Coil Steam Generator," *Transactions of the Korean Nuclear Society Autumn Meeting*, Jeju, Korea, October 21-22, 2010, pp.47 (2010).
5. J.N. Reyes Jr., "NuScale Plant Safety in Response to Extreme Events," *Nuclear Technology*, **178**, pp. 153-163 (2017). DOI: 10.13182/NT12-A13556
6. E.U. Schlünder, *Heat Exchanger Design Handbook*, Washington: Hemisphere Publishing Corporation, 1983. Print.
7. H.B. Seo, T.Y. Ryu, Y.J. Kim, Y.S. Chang, J.W. Kim, and T.W Kim, "Limit Load Analyses of Helical Coiled Steam Generator Tubes with a Volumetric Flaw," *Fatigue & Fracture of Engineering Materials and Structures*, **35**, pp. 1022 – 1032, (2012).
8. R.P. Wallis, "A photographic study of fluid flow between banks of tubes," *Proceedings of the Institution of Mechanical Engineers*, **142** (1939).

9. P. Bradshaw, "The effect of wind tunnel screens on nominally two-dimensional boundary layers," *Journal of Fluid Mechanics*, **22**, pp. 679-687, (1965).
10. M.M. Zdravkovich, "Smoke Observation of Wake of Tandem Cylinders," *The Aeronautical Journal*, **76**, pp. 108-114, (1972).
11. D.S. Weaver, and A. Avd-Rabbo, "A flow visualization study of a square array of tubes in water cross flow," *ASME Journal of Fluids Engineering*, **107**, pp.354-363 (1985).
12. S. Aiba, H. Tsuchida, and T. Ota, "Heat Transfer around Tubes in Staggered Tube Banks," *JSME International Journal of Fluids and Thermal Engineering*, **25**, pp. 527-533, (1982).
13. O. Simonin, and M. Barcouda, "Measurements and predictions of turbulent flow entering a staggered tube bundle," *Proceedings of 4th International Symposium on Applications of Laser Anemometry to Fluid Mechanics*, Lisbon, Portugal, July 11 – 14, 1988, pp. 5.23, (1988).
14. S. Balabini, and M. Yianneskis, "Vortex Shedding and Turbulence Scales in Staggered Tube Bundle Flows," *Canadian Journal of Chemical Engineering*, **75**, pp.823- 831, (1997).
15. Y.A. Hassan, and H.R. Barsamian, "Tube bundle flows with the large eddy simulation technique in curvilinear coordinates," *International Journal of Heat and Mass Transfer*, **47**, pp. 3057 (2004).
16. C. Sweeny and C. Meskell, "Fast numerical simulation of vortex shedding in tube arrays using a discrete vortex method," *Journal of fluids and structures*, **18**, pp. 501 (2003).
17. A. Cioncolini, and L. Santini, "Two-phase pressure drop prediction in helically coiled steam generators for nuclear power applications," *International Journal of Heat and Mass Transfer*, **100**, pp. 825 – 834, (2016).
18. A.A. Zukauskas and R.V. Ulinskas, *Heat Transfer in Tube Banks in Crossflow*, Hemisphere Publishing Corporation, New York USA (1988).

19. S.S. Paul, M.F. Tachie, and S.J. Ormiston, "Experimental study of turbulent cross-flow in a staggered tube bundle using particle image velocimetry," *International Journal of Heat and Fluid Flow*, **28**, pp. 441- 453, (2007).
20. C. Iwaki, K.H. Cheong, H. Monji, and G. Matsui, "PIV Measurement of the vertical cross-flow structure over tube bundles," *Experiments in Fluids*, **37**, pp. 350-363, (2004).
21. E. Konstantinidis, S. Balabani, and M. Yianneskis, "A study of vortex shedding in a staggered tube array for steady and pulsating cross-flow," *Trans. ASME Journal of Fluids Engineering*, **124**, pp. 737-746, (2002).
22. D.K. Williams, D.P Fassett, B.J. Webb, W.J. Bees, and A.S. Kruskamp, "Helical Coil Steam Generator," U.S. Patent 20120111287 A1, Issued Apr. 12, 2013. (2013).
23. M. Esch, B. Jurgens, A. Hurtado, D. Knoche, and W. Tietsch, "State of the Art Helium Heat Exchanger Development for Future HTR-Projects," *Proceedings of the 2008 International Topical Meeting on High Temperature Reactor Technology (HTR-2008)*, Washington, DC, September 28- October 1, 2008, (2008).
24. J.K. Lai, E. Merzari, S.J. Lee, M. Delgado, S. Lee, and Y.A. Hassan, "Large Eddy Simulations for a Helical Coil Steam Generator," *Proceedings of the 2016 International Topical Meeting on High Temperature Reactor Technology (HTR-2016)*, Las Vegas, NV, November 6–10, 2016, pp.1655, (2016).
25. A. Kraus, H. Yuan, and E. Merzari, "Simulations of a Helical Tube Bundle in Cross-Flow for Application to Flow-Induced Vibration," *Proceedings of the 2016 ANS Winter Meeting and Technology Expo*, Las Vegas, NV, November 6–10, 2016, pp.1668 (2016).
26. S. B. Beale and D.B. Spalding, "A Numerical Study of Unsteady Fluid Flow in In-line and Staggered Tube Banks," *Journal of Fluids and Structures*, **13**, pp. 723, (2011).

27. R.D Mehta, and P. Bradshaw, “Design rules for small low speed wind tunnels,” *The Aeronautical Journal of the Royal Aeronautical Society*, **718**, pp. 443 – 449, (1979).
28. C. Fort, C.D. Fu, N.A. Weichselbaum, P.M. Bardet, “Refractive Index and solubility control of para-cymene solutions for index-matched fluid structure interaction studies,” *Experiments in Fluids*, **56**:210, (2015).
29. P. Liu, H. Zhang, Y. Wu, M. Zhang, and J. Lu, “Experimental study on the flow interaction of two parallel rectangular jets through exits with sudden contraction,” *Experimental Thermal and Fluid Science*, **89**, (2017).
30. S.J. Lee, S. Lee, Y. A. Hassan, “Numerical Investigation of the Flow Inside the Helical Coil Steam Generator Test Section,” Proceedings of the 2016 International Topical Meeting on High Temperature Reactor Technology (HTR-2016), Las Vegas, NV, November 6–10, 2016, (2016).
31. C. Brossard, J.C. Mannier, P. Barricau, F.X. Vandernoot, Y. Le Sant, F. Champagnat, G. Le Besnerais, “Principles and Applications of Particle Image Velocimetry,” *Aerospace Lab Journal*, **1** (2009).
32. ITTC, “ITTC – Recommended Procedures and Guidelines: Guideline on the Uncertainty Analysis for Particle Image Velocimetry,” *International Towing Tank Conference Proceedings*, **7.5-01-03-03** (2014), 1-18.
33. E. Guillou, M. Gancedo, E. Gutmark, A. Mohamed, “PIV investigation of the flow induced by a passive surge control method in a radial compressor”, *Exp. Fluids*. **53** (2012) 619–635.
34. M. Immer, J. Allegrini, and J. Carmeliet. “Time-resolved and time-averaged stereo-PIV measurements of a unit-ratio cavity,” *Experimental Fluids*, **57**(101), (2016).

35. S. Lee, Y.A. Hassan. “Experimental study of flow structures near the merging point of two parallel plane jets using PIV and POD,” *International Journal of Heat and Mass Transfer*, **116** (2018) 871-888.
36. P. Sabharwall, T. Conder, R. Skifton, C. Stoots, and E.S. Kim, “PIV Uncertainty Methodologies for CFD Code Validation at the MIR Facility,” Technical Report INL/EXT-12-27728, (2013).
37. M. Delgado, S. Lee, Y. Hassan, N.K Anand, “Flow visualization study at the interface of alternating pitch tube bundles in a model helical coil steam generator using particle image velocimetry,” *International Journal of Heat and Mass Transfer*, **122** (2018) 614 – 628.